Oxygen atom and ozone kinetics in the afterglow of a pulse-modulated DC discharge in pure O2 : an experimental and modelling study of surface mechanisms and ozone vibrational kinetics

Jean-Paul Booth, Olivier Guaitella, Shu Zhang, Dmitry Lopaev, S Zyryanov, T Rakhimova, D Voloshin, Alexander Chukalovsky, Andrey Vladimirovich Volynets, Yu Mankelevich

Oxygen atom and ozone kinetics in the afterglow of a pulse-modulated DC discharge in pure O_2: an experimental and modelling study of surface mechanisms and ozone vibrational kinetics

J-P. Booth[1], O. Guaitella[1], S. Zhang[1], D. Lopaev[2], S. Zyryanov[2], T. Rakhimova[2], D. Voloshin[2], A. Chukalovsky[2], A. Volynets[2], Yu. Mankelevich[2]

[1] *Laboratoire de Physique des Plasma (LPP), CNRS, Sorbonne Université, École Polytechnique, Institut Polytechnique de Paris, 91120 Palaiseau, France*

[2]*Skobeltsyn Institute of Nuclear Physics, Lomonosov Moscow State University, Russian Federation*

Abstract

The chemical kinetics of oxygen atoms and ozone molecules were investigated in a fully-modulated DC discharge in pure oxygen gas in a borosilicate glass tube, using cavity ringdown spectroscopy (CRDS) of the optically forbidden $O(^3P_2) \rightarrow O(^1D_2)$ absorption at 630nm. Measurements were made over a range of tube temperatures (10 and 50°C) gas pressures (0.5-4 Torr) and discharge current (10-40 mA). The discharge current was square-wave modulated (on for 0.2 seconds and off for 1 second), allowing the build-up to steady-state and the decay in the afterglow to be studied. This paper focusses on the afterglow period. The O atom density decays non-exponentially in the afterglow, indicating a surface loss probability dependent on incident active particle fluxes. The oxygen atom absorption peak lies on a time-varying absorption continuum due (in the afterglow) to the Chappuis bands of ozone. The ozone density passes through a maximum a few 100ms into the afterglow, then decays slowly. An existing time-resolved self-consistent 1D radial model of O_2 positive column discharges was modified to interpret the new results. The ozone behaviour in the afterglow can only be modelled by the inclusion of : 1) surface production of O_3 from the reaction of O_2 molecules with adsorbed O atoms, 2) reactions of vibrationally-excited ozone with O atoms and with $O_2(a^1\Delta_g)$ molecules, and 3) surface loss of ozone with a probability of around 10^{-5}.

1. Introduction

Electrical discharges in oxygen gas, both at low pressure and at atmospheric pressure, have been the subject of many experimental and theoretical studies over the years. The radicals, ions and other active species produced in them are useful for many applications including: cleaning of various surfaces [1], sterilisation of medical devices [2], plasma-based water treatment [3], chemical vapour deposition of metal oxide films [4], etching of various materials and resist stripping in microelectronics [5]. Numerous gas-phase and surface reactions [6, 7] are involved in the production and loss of the important active species, including oxygen atoms and ozone molecules which are the focus of this study. Various techniques have been developed to probe oxygen atom concentrations: VUV absorption [8-11], optical emission [12], optical emission actinometry [9, 13], two-photon laser induced fluorescence [14], and, most recently, cavity ringdown spectroscopy (CRDS) [15].

This study is a continuation of a series of studies of DC positive column discharges in pure oxygen gas, using a range of different diagnostic techniques on the same basic discharge configuration [6, 16, 17]. The positive column region of DC discharges is very suitable for investigation of elementary processes because it can be operated in a regime where the axial electric field (and other parameters such as gas composition and temperature) is uniform. In this case, only the radial dependence of the discharge properties need to be taken into account, and a 1D(r) numerical simulation can be used. Although measurements were made in both the active plasma and the afterglow, this article will focus on the afterglow results.

The ozone molecule possesses three vibrational modes, the symmetric stretch ν_1 (1135 cm^{-1}), the bending mode ν_2 (716 cm^{-1}), and the asymmetric stretch ν_3 (1089cm^{-1}). The recombination of oxygen atoms with oxygen atoms to form ozone passes through the creation of vibrationally-excited ozone, $O_3^{\ddagger}$:

$$O + O_2 \rightleftarrows O_3^{\ddagger} \xrightarrow{M} O_3 \qquad (1)$$

The excess energy released in the first stage of this reaction is 106 $kJmol^{-1}$ (1.09eV, 8860cm^{-1}), indicating that many vibrational states can be populated in this reaction. The formation of vibrationally-excited ozone in this reaction was observed in 1973 by von Rosenberg and Trainor [18]. At atmospheric pressure these excited ozone molecules are quickly quenched by collisions with the bath gas, M (in the atmosphere these would be N_2 or O_2 molecules), leading to the formation of ground-state ozone, with the well-established rate coefficient $6x10^{-34}.(T/300)^{-2.3}cm^6s^{-1}$ given by Lin and Leu [19]. However, when the gas is strongly dissociated and activated, such as under lower-pressure plasma conditions, $O_3^{\ddagger}$ can also react with other species such as O_2(a) [20], and O(^{3}P) (first observed by West et al. [21], and studied in more detail by Rawlins et al. [22]) before

vibrational quenching can occur. In this case the yield of (ground state) ozone is decreased, in favour of other products, notably ground-state oxygen molecules.

Klopovskii et al. [23, 24] observed the decay of $O_2(a^1\Delta_g)$ in the discharge afterglow, and explained the results with a model which included vibrationally excited ozone and its reactions with $O_2(a)$. They assumed separate vibrational temperatures for the stretching and bending modes. Vlasov et al. [25] used this scheme to explain the altitude profile of $O_2(a)$ in the upper atmosphere.

Lopaev et al. [26] studied an O_2 DC discharge at 10–50 Torr, using the Hartley band absorption to probe the ozone density and vibrational temperature, and interpreted the results using a 1D reaction model for gas-phase and surface processes. They proposed a model considering excitation of the asymmetric stretch up to $O_3(0,0,2)$. The activation energies for the reactions of these states were assumed to reduce progressively with the vibrational energy.

Marinov et al. [27] studied pulsed direct current oxygen discharges at 1–5 Torr pressure, making time-resolved measurements of the absolute concentrations of ground-state O atoms (by two-photon absorption laser-induced fluorescence) and ozone molecules (by ultraviolet absorption of the Hartley band, centred at $\lambda = 255$ nm). They interpreted their results with a self-consistent model including vibrationally excited ozone, assuming one effective vibrationally-excited O_3 state, $O_3(v)$. They concluded that the reactions of $O_3(v)$ with atomic oxygen and $O_2(a^1\Delta_g)$ metastables are significant, leading to a decrease in the overall ozone production (compared to that expected from the well-established three-body reaction rate constant [19]) by factor of ~2 in the pressure range 1-5 Torr in the afterglow of a DC positive column discharge. They concluded that ozone formation at the wall did not contribute significantly to the total ozone production under their conditions. However, their discharge tube was not cooled; the present results show that ozone production is strongly enhanced at lower wall temperature.

Azyazov et al. [28, 29] studied the dynamics of $O_2(a)$ and O_3 following pulsed laser photolysis experiments in O_3/O_2 and $Ar/O_3/O_2$ mixtures at pressures in the range 400-712 Torr. They interpreted their experimental results with a model comprising a single effective vibrational quantum number, $v_{eff}=(v_1+v_2+v_3)$. They assumed that in the first step of reaction (1) vibrational energy accumulates mainly in the stretching modes of O_3, with $v_{eff} \geq 2$. The rates of reaction of $O_3(v_{eff})$ with $O(^3P)$ and $O_2(a)$ were then expressed as a function of the vibrational energy. When the vibrational energy exceeds the activation energy of a specific reaction, the rate was assumed to be constant. For the reaction with $O(^3P)$ atoms this condition is fulfilled for $v_{eff} \geq 2$. The branching ratio for the production of O_2 was assumed to be $\gamma \sim 0.81$, with the remainder going to relaxation : $O_3(v)+O \rightarrow O_3 + O$. The reaction with $O_2(a)$ was also included with a rate constant of $k_{20} = 4.1 \cdot 10^{-11}$ cm^3 s^{-1}.

Following on the progress made in previous studies [26, 27], the purpose of this study is to obtain better quantitative data under well-controlled conditions (stabilised wall temperature and lower pressures), allowing a detailed study of the mechanisms of surface O_3 production and loss as well as a quantitative understanding of the effect of vibrational states on ozone build-up in the afterglow. We present new CRDS measurements of the dynamics of O and O_3 in pulsed O_2 dc discharges and their afterglow, over a range of discharge parameters (gas pressure p, discharge current I_d and Pyrex tube temperature T_w). These time-resolved experimental data allow thorough testing of O_2 plasma models. As suggested by the previous studies [26, 27], our present experimental results can only be explained with the inclusion of both detailed ozone vibrational kinetics and of ozone surface (production and loss) processes, coupled with atomic oxygen surface reactions. In this paper, these processes are examined in more detail and incorporated into an existing 1D radial model of the positive column of O_2 discharge [16, 17]. The model results are compared to six experimental discharge regimes, and tested for both the discharge and post-discharge modes.

This article is organized as follows. Section 2 describes the experimental setup and the diagnostic techniques employed. Section 3 presents the experimental results obtained. Section 4 describes the additions to the 1D model related to ozone surface and volume processes. Section 5 discusses the experimental results in comparison with the model.

2. Experimental techniques

The experimental setup is shown in Figure 1. The discharge tube is the same as that used in previous studies [6, 16, 17], and so will only be briefly described here. The inner diameter of the tube is 20 mm. The discharge is ignited between two cylindrical electrodes, separated by 54 cm, placed in side-arms of ~3 cm length, so that the main tube where the CRDS measurements are made contains only the positive column region. The temperature of the tube surface can be kept constant by a water/ethanol mixture flowing through an outer envelope and connected to a thermostatic bath. The anode is connected to a positive polarity high voltage power supply via a non-inductive, while the cathode is connected to ground via a non-inductive. The electric field in the positive column was measured by two floating high-impedance probes [6, 17]. For kinetic measurements the high voltage power supply was fully (100%) modulated providing pulsed discharge. The experiments were carried out in the pressure range 0.5-4 Torr and currents I_d=10-40mA. The wall temperature was varied from +10°C to +20°C. Prior to kinetic measurements the discharge was run under standard conditions (1 Torr, 40mA, wall temperature 20°C) to stabilise the wall conditions.

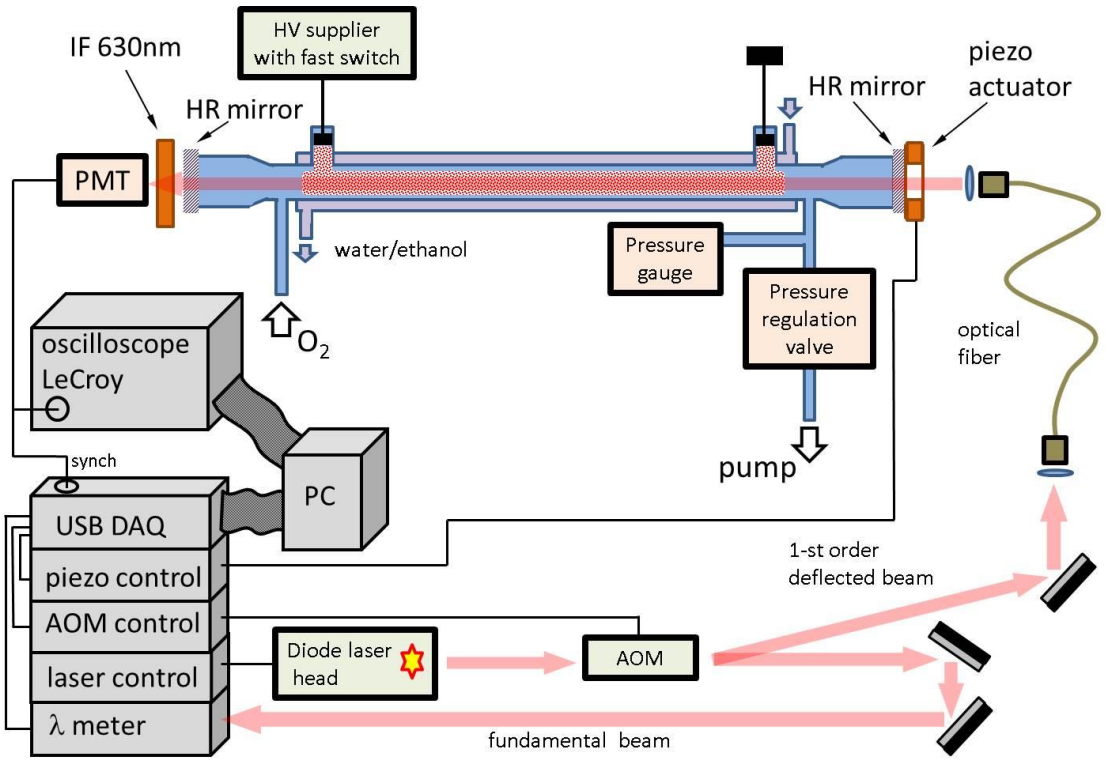

Figure 1. Experimental set up.

The column-integrated density of oxygen ^3P atoms, as well as their translational temperature, were determined by cavity ringdown spectroscopy (CRDS) of the forbidden $^3P_2 \rightarrow {}^1D_2$ transition at 630.205 nm as developed by Peverall et al. [15] using an optical setup described previously [16]. The ringdown cavity comprises two concave (R=1 metre) high-reflectivity dielectric mirrors separated by 68cm. The absorption length comprises the positive column zone of length L≈54 cm (at $0 \leq z \leq 54$ cm) and two 'dead' end-zones each of length $L_{dz} \approx 7$ cm (at $-7<z<0$ and $54<z<61$ cm). The characteristic radiation decay time in the empty cavity, τ_0, was typically about 15μs. Tuneable radiation from a narrow-band diode laser (Toptica DLPro) is passed through an Acousto-Optic Modulator (AOM). The first order of diffraction is injected into an optical fiber, and the output of the fiber is injected in to the cavity through the entrance mirror after adjusting the laser beam divergence and focus (with an 11mm focal length lens) to optimise transverse mode matching to the cavity. The radiation exiting the cavity is passed through a 630nm interference filter and detected by a photomultiplier (Hamamatsu R928). The experiment is controlled by a NI Labview™ program running on a PC. The PMT signal was digitised using a national Instruments USB 6356 A/D converter (1.25 MS/s) controlled by computer. The laser wavelength is continuously monitored by a wavemeter (HighFinesse WS-U).

The spectral width of the laser line is significantly narrower than the cavity longitudinal mode spacing. Therefore, longitudinal mode matching is achieved by scanning of the cavity length

with a piezo-actuator attached to the output mirror. When the laser wavelength and longitudinal mode coincide, laser radiation enters the cavity, and signal is detected at the PMT. When the detected intensity passes an adjustable threshold a ringdown event starts; the AOM is shut off (for 1 ms) and the exponential decay time, τ, is determined by numerical fitting. The linear absorption coefficient, α (in cm^{-1}), averaged over the cavity length, is then calculated from:

$$\alpha = \frac{1}{c}.\left(\frac{1}{\tau} - \frac{1}{\tau_0}\right)$$

where c is the speed of light.

With this setup it is not possible trigger the ringdown events in order to synchronise them with the discharge pulsing. However, the kinetics of oxygen atoms and ozone is rather slow (see below) compared to the ringdown times. Therefore the ringdown process was allowed to free-run (with typically about 30 events per second), and the phase delay between each event and the start of the pulse cycle was recorded. After accumulation of an adequate number of events (several 10's of minutes) the results are sorted into time bins (1-5 ms wide), providing time-resolved measurements through the discharge pulse sequence.

The (Doppler-broadened) oxygen atom $^3P_2 \rightarrow {}^1D_2$ absorption peak lies on top of an absorption continuum that is due to both ozone and O^- negative ions (discussed in detail below). Therefore the time-varying oxygen atom density is determined by measuring the absorption at the peak of the transition (referred to as the "on-resonance absorption") and subtracting the (time-varying) absorption measured at a slightly shifted (about $0.15cm^{-1}$) laser wavelength (referred to as the "off-resonance absorption")

For continuous plasma measurements, the laser is scanned over the Doppler profile of the atomic absorption line, giving the linear absorption coefficient, α(ν) as a function of the laser frequency, ν. This profile is fitted (using a non-linear least squares algorithm) by a Gaussian function, giving the integrated linear absorption coefficient, $\int \alpha . d\upsilon$, and the Doppler width, $\Delta\upsilon_D$. The gas translational temperature is calculated directly form this Doppler width. The number density of oxygen atoms in the $^3P_2$ state, $[O(^3P_2)]$ is calculated from: $[O(^3P_2)] = \int \alpha . d\upsilon / \sigma_{int}$, where σ_{int} is the integrated absorption cross-section for the transition. This is related to the Einstein A coefficient of transition, A_{low}^{up}, by :

$$\sigma_{\text{int}} = \int \sigma_{low}^{up} d\nu = \frac{g_{up}}{g_{low}} \frac{A_{low}^{up} \lambda^2}{8\pi}$$

where g_{up} and g_{low} are the degeneracy of the upper and lower states (both equal to 5 in this case). The Einstein A coefficient of the $^3P_2 \rightarrow {}^1D_2$ transition is known only from theoretical calculations, with a value of $5.65 \times 10^{-3} s^{-1}$ according to the NIST atomic spectra database [30], with an estimated uncertainty of ±7%, corresponding to $\sigma_{int} = 2.977 \times 10^{-23}$ cm^2/cm^{-1}.

For time-resolved measurements, only the absorption at the peak of the Doppler profile is measured. The peak absorption cross-section is given by $\sigma_0[cm^2]=9.846\times10^{-21}/T_g^{0.5}$. Peverall et al. [15] observed that the populations of the $O(^3P_J)$ states are close to equilibrium with the gas translational temperature in an inductively-coupled discharge in pure O_2 at 100 mTorr. At the higher gas pressures studied here the collisional equilibration of spin-orbit levels will be even faster, so it is safe to assume that the spin-orbit levels will again be in equilibrium with the gas translational temperature. Therefore, the total number density of O (^3P) atoms can be calculated from the $O(^3P_2)$ density using the relation:

$$[O(^3P)] = [O(^3P_2)]\frac{1}{g_2}\sum_J g_J e^{-E_J/kT}$$

Here g_J = 5, 3, 1 and E_J = 0, 227.67, 326.5 K for J = 2, 1 and 0, respectively.

3. Experimental results.

Figures 2-5 show, for a range of gas pressures, discharge currents and tube wall temperatures, the observed dynamics of (a) the absorption by oxygen atoms (measured at the peak of the resonance, with the off-resonance contribution subtracted) and (b) the off-resonance absorption. The discharge was on for the period $-0.2<t\leq 0$ and off for the period $0<t<0.8$ s. Note that the values presented here represent the linear absorption coefficient averaged over the distance between the two mirrors, including the end-zones with no discharge.

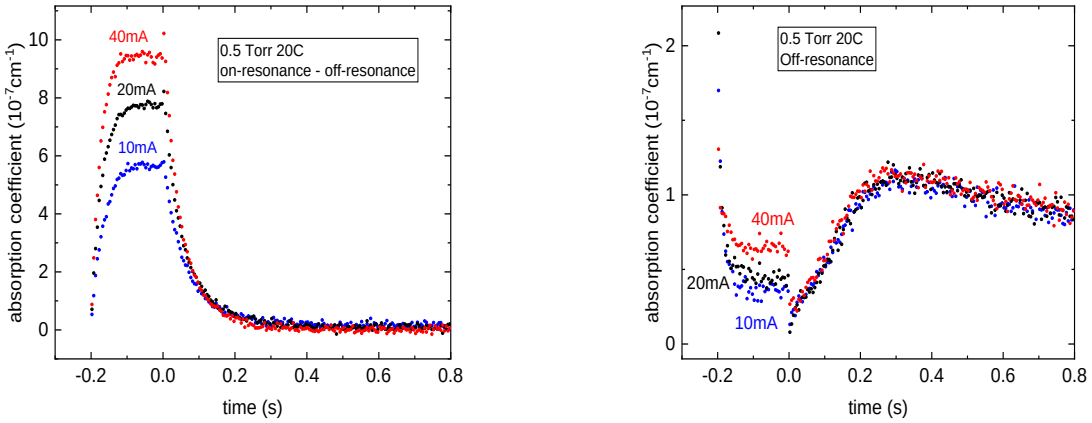

Figure 2. (a) Absorption at the peak of the oxygen atom transition (background subtracted) and (b) off-resonance absorption, at p=0.5 Torr, T_w=+20°C and discharge currents I_d=10, 20 and 40 mA.

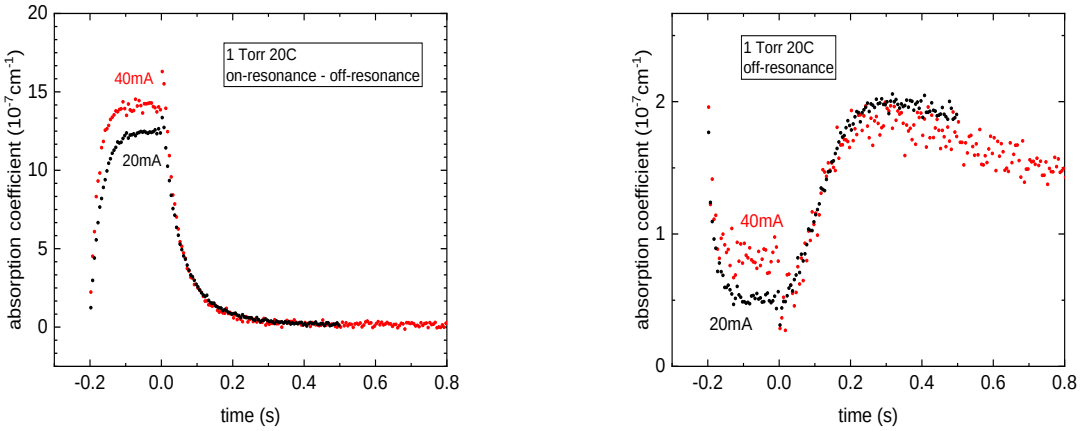

Figure 3. (a) Absorption at the peak of the oxygen atom transition (background subtracted) and (b) off-resonance absorption, at p=1 Torr, T_w=20 C and discharge currents I_d=20 and 40 mA.

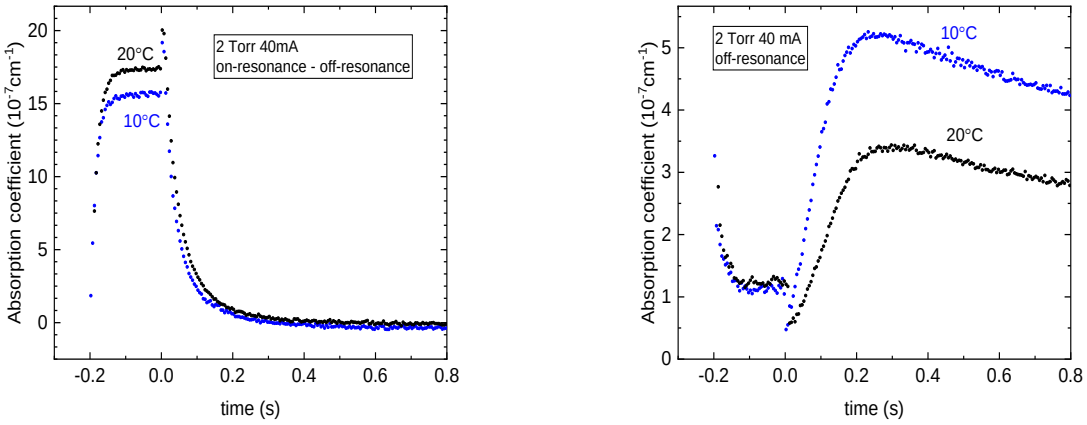

Figure 4. (a) Absorption at the peak of the oxygen atom transition (background subtracted) and (b) off-resonance absorption, at p=2 Torr, T_w=10°C and 20°C and I_d= 40 mA.

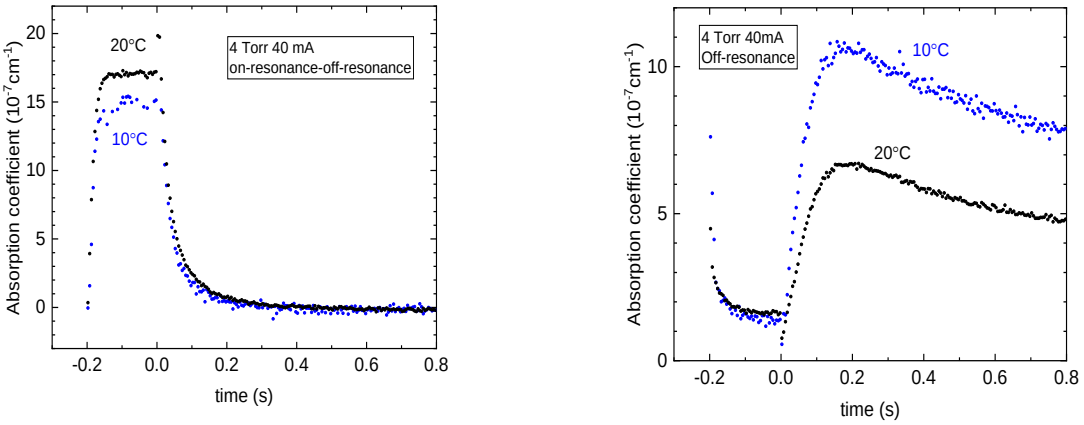

Figure 5. (a) Absorption at the peak of the oxygen atom transition (background subtracted) and (b) off-resonance absorption, at p=4 Torr, I_d=40 mA, T_w=10°C and 20°C.

During the steady-state active discharge the gas temperature (determined from the Doppler width of the oxygen transition) is higher than the temperature of walls of the borosilicate tube, and increases with both discharge current and pressure, reaching 566±11K at the discharge axis for 4 Torr 40mA. After discharge extinction the radial gas temperature profile relaxes to a uniform profile in equilibrium with the wall temperature. Time-resolved measurements of the Doppler absorption profile of the $O(^3P_2)\rightarrow O(^1D)$ line (not presented here) have shown that this occurs in less than 3 ms (and faster at the lower pressures), in agreement with an analytical calculation using the gas heat capacity and conductivity. This rapid drop in the axial temperature causes an initial fast increase ("jump") in the observed O atom absorption, due to two effects: 1) the Doppler width narrows, increasing the peak absorption cross-section, and 2) the $O(^3P_2)$ concentration at the axis increases, due to a flux of gas from the region near the walls towards the axis as the radial temperature profile becomes uniform. Subsequently the $O(^3P_2)$ absorption decays over a longer

time-scale, as seen in Figures 2a-5a. Even after the temperature equilibration, the $O(^3P)$ decay is not single-exponential; it is initially faster, but slows down further into the afterglow. This can be seen in the semi-logarithmic plots shown in section 5, figure 8-12. Possible reasons for this behaviour will be discussed in section 5.

Now let us consider the temporal behaviour of the "off-resonance" continuum absorption, $\alpha_{\text{off-resonance}}$, observed when the laser is tuned away from the oxygen transition. There are two species present in oxygen discharges which show continuum absorption in this spectral region, ozone (the Chappuis bands, $\sigma_{O3}=3.6\times10^{-21}$ cm^2 at 630nm [31, 32]) and O^- negative ions (photodetachment continuum, $\sigma_{O^-}=5.8x10^{-18}$ cm^2 at 630nm [33]). However, oxygen negative ions are only present in the active discharge, since they are destroyed quickly by associative detachment reactions with O atoms and $O_2(a)$ molecules [34, 35], and disappear within a few microseconds after discharge extinction. Conversely, the ozone concentration in the active discharge is very small because it is destroyed efficiently by electron-impact dissociation, and also thermally decomposes at higher gas temperatures (see Section 5). Immediately after discharge extinction, the off-resonance absorption drops sharply (within one sampling gate of duration 1 ms), almost (but not quite) to zero, due to the disappearance of the negative ions. The residual absorption observed can be attributed to ozone which has accumulated in the end-zones. After this, the off-resonance absorption rises slowly, passing through a maximum before decaying slowly (with a time constant of about 500ms). The maximum occurs after about 300ms at 0.5 Torr, and at earlier times at higher pressures (for example, about 150 ms at 4 Torr) (Figures 2b-5b). This continuum absorption in the afterglow can be attributed solely to ozone, since the negative ions have disappeared. It is therefore a direct measure of the average ozone axial density $[O_3(0,0,0)](r=0,t)$. Given this observed long ozone lifetime, it will have time to diffuse across the tube, giving a spatially uniform distribution in the afterglow. Therefore the ozone concentration is given by $[O_3(0,0,0)] = \alpha_{\text{off-resonance}}/\sigma_{O3}$.

The ozone density in the afterglow is only slightly affected by value of the discharge current (see figs 2b and 3b), implying that the dominant production mechanism does not directly involve active species such as oxygen atoms. However, the O_3 density does increase markedly with gas pressure, and is also significantly higher with a wall temperature of 10C compared to 20C. These observations are not consistent with gas-phase production of ozone through reaction (1), which in any case cannot account for the quantity of ozone produced at the lower pressures (2 Torr and below). The results therefore indicate surface production of ozone by the reaction of molecular O_2 (hence the pressure dependence) with adsorbed oxygen atoms. Ozone production mechanisms will be discussed further below.

4. Model

4.1 Model overview

The model employed here was developed from an existing model for N_2 and O_2 dc discharges [36, 37]. It is a fluid model with one-dimensional radial geometry, and can simulate both steady-state and time-resolved behaviour. The model resolves the non-stationary conservation equations for neutral and charged species $n_i(r,t)$ and the heat transfer equation for gas temperature $T_g(r,t)$. The electron energy distribution function (EEDF) f(ε,r,t) is calculated by solving the Boltzmann kinetic equation in the two-term approximation as a function of the reduced electric field, E/N. It includes a full set of chemical reactions for ions and neutrals. These equations are solved numerically with a constant time step of Δt~40 ns up to the steady state condition for each given set of discharge current I_d and axial electric field $E(t=0)$. With set initial (at t=0) and boundary (at r=0 and R_t) conditions. During the calculation process, $E(t=0)$ was continuously adjusted to keep a constant nominal discharge current, I_d. All of the reactions in the mechanism are processed by the chemical translator to form and to recalculate the reaction rates for all species (source and loss terms). Radial diffusion, drift and loss at the tube wall are calculated for charged species. As the gas mixture changes, the electron energy distribution function (EEDF) f(ε,r,t) is also recalculated. This study is principally concerned with analysis of the kinetics in the afterglow. In order to model this, the simulation is first run up to steady state conditions. This data is then set as the initial conditions for the time-resolved simulations of the afterglow, with the current set to zero.

The kinetic scheme concerns both charged species (electrons, positive ions O^+, O_2^+, O_4^+, and negative ions O^-, O_2^-, O_3^-) and neutral species ($O(^3P)$, $O(^1D)$, $O(^1S)$, O_3, $O_2(a^1\Delta_g)$ (further denoted as $O_2(a)$), $O_2(b^1\Sigma_g^+)$ (further denoted as $O_2(b)$), O_2**(Herzberg states) and ground state $O_2(X^3\Sigma_g^-,v)$ for vibrational levels v=0-32). The reaction set is based on the one presented in Booth et al. [16], but with the addition of the kinetics of vibrationally-excited ozone (Section 4.3) as well as surface production and loss processes for ozone (Section 4.2, 5.3 and 5.4). This scheme is described in detail in papers [16, 17, 37].

The model was used to describe six experimental discharge regimes:

Regime	**p, Torr**	**T_w, °C**	***I*, mA**
1	0.5	20	40
2	1	20	40
3	2	20	40
4	4	20	40
5	4	10	40
6	1	20	20

The effect of pressure at fixed T_w = 20°C and discharge current of 40 mA are investigated in regimes 1-4 (pressures p = 0.5, 1, 2, 4 Torr). The effect of wall temperature (T_w = 10°C and 20°C) is seen by comparing regimes (4) and (5) at 4 Torr, 40 mA. The effect of discharge current (I = 20 mA and 40 mA) is seen by comparing regimes (5) and (6) at 1 Torr, T_w = 20°C.

4.2. Surface processes

4.2.1 O atom surface loss

During the active discharge, O ^{3}P atoms are predominantly lost by surface processes, and gas phase reactions play only a minor role except at the highest pressures [17]. Therefore, the observed non-exponential decay of O atoms in the afterglow indicates that the surface reaction probability, γ_O, is not constant, but becomes smaller with time in the afterglow. A previous study of oxygen atom recombination on borosilicate glass surfaces [17] found that the surface reaction probability (at a given tube temperature, T_w) can be described by a function comprising two terms, a constant term, γ_O^1 (which on its own would lead to a single exponential decay) and an additional term proportional to the oxygen atom flux, expressed in the form:

$$\gamma_O = \gamma_O^1 + \gamma_O^2 \times [O]/10^{15}[cm^{-3}]$$

The constant term, γ_O^1, can be attributed to an Eley-Rideal reaction of incident oxygen atoms with chemisorbed oxygen atoms (with a constant surface density). The second term, $\gamma_O^2 \times [O]/10^{15}[cm^{-3}]$ (where [O] is O(^{3}P) atom density near the tube wall (in units of [cm^{-3}]) and 10^{15}[cm^{-3}] is a the scale factor), is proportional to the incident O(^{3}P) flux. This term represents gas-phase oxygen atom reaction with more weakly-bound (quasi-physisorbed) oxygen atoms, whose surface density will be proportional to the incident flux[17]. Since gas-phase reactions also make a small contribution to the O(^{3}P) loss (especially at the higher gas pressures), the values of γ_O^1, and γ_O^2 were determined by adjusting their values in the simulation until the simulated oxygen atom densities match the observations, both in the steady state and the afterglow. The values used in the simulation for each set of experimental conditions are summarized in Table 3, with the values for γ_O^1 lying in the range (3.2-3.7)x10^{-4}, and for γ_O^2 in the range (1.1-2.9)x10^{-4}. These surface reaction parameters (in particular γ_O^1) were observed to vary somewhat depending on the history of the tube, especially as a function of the discharge running time after an overnight shut-down, therefore the discharge was operated for at least an hour before kinetic measurements were taken.

4.2.2 O_2(a) and O_2(b) surface loss

The kinetics of O_2(a) were not measured in this study; however they have been measured previously in a similar discharge tube (using both IR emission and vacuum ultraviolet absorption [6]). The O_2(a) density was observed to decay almost exponentially, but again a little faster at the beginning of the afterglow, with a lifetime in the region of 140-200ms, depending only weakly on the gas pressure and discharge current. Therefore, in the model the surface loss of O_2 ($a^1\Delta_g$) was represented by a similar expression to that used for oxygen atoms: $\gamma_{O2a}= \gamma^1_{O2a}+ \gamma^2_{O2a}\times[O]/10^{15}$.

In the active discharge the kinetics of O_2 ($a^1\Delta_g$) are dominated by electron-induced processes:

Excitation/de-excitation:

$O_2(X)+e \leftrightarrow O_2(a)+e$,

$O_2(a)+e \leftrightarrow O_2(b)+e$,

Dissociation:

$O_2(a)+e \rightarrow 2O(^3P)+e$

Surface loss, as observed in the afterglow, plays only a minor role in the active discharge. Reactions with ground-state ozone represent a negligible loss pathway for O_2 ($a^1\Delta_g$).

The O_2(b) surface loss probability was assumed to be constant, with the value of γ_{O2b} = 0.135, determined in a previous study [17] from time-resolved optical emission spectroscopy in a similar discharge tube.

4.2.3 Ozone surface loss

The loss rate of ground-state ozone is treated, for computational convenience, as an effective ozone surface loss probability γ_{O3} representing surface reaction and a contribution due to gas flow. The gas flow (the average flow velocity v_a = 87 cm/s for p=0.5 Torr, T_w=20 C and a flow rate of 10 sccm) will make some contribution to the loss of ozone especially at low pressures. However, this loss is not simply proportional to the gas flow velocity, v_a, because of ozone diffusion into the perpendicular side-tubes of the discharge tube including the upstream gas flow tube. The values of γ_{O3} are adjusted in the simulation to fit the observed ozone decay at long times. The values used are presented later (section 5.1), and lie in the range (0.3-0.5)x10^{-4}.

4.2.4 Ozone surface production

Several previous studies have shown evidence for surface production of O_3, and proposed various models for it. Marinov et al.[27, 38] and Lopaev et al. [26] proposed models with ozone production proportional to the incident O atom flux. Lopaev et al. [26] also proposed surface production of O_3 on fused silica by the recombination of O_2 with quasi-physisorbed O atoms, and Mazánková et al. proposed a similar mechanism on alumina and copper surfaces [26, 39]. We

compared the results of different surface ozone production models with the present experimental results: 1) proportional to O atom flux and 2) proportional to the O_2 flux. Only the latter matches the observed dynamics of O_3 in the afterglow.

Therefore, we used a model in which the O_3 flux produced at the surface, (FS_{O3}), is proportional to the incident O_2 flux with the following functional form (discussed later in Section 5.3):

$$FS_{O3} = ab[O_2]/(1+b[O_2]/[O]),$$

where the $[O_2]$ and [O] are the concentrations near the wall. The two model parameters (*a* and *b*) were adjusted to fit the observed dependence of the $[O_3(CRDS)](t)$ dynamics at low and high pressures, giving ab=0.019, b=0.016. The same values were used for all regimes studied in this paper.

4.3. Kinetic scheme for vibrational excited ozone.

4.3.1 Vibrational scheme with effective levels

The energy released by the recombination of O atoms with O_2 molecules (1.09eV) is sufficient to populate a large number of vibrational states involving all three vibrational modes $O_3(v_1, v_2, v_3)$. These different nascent states will have different reaction rates, and will undergo stepwise collisional relaxation. However, a complete state-resolved model of the kinetics of vibrationally-excited ozone would require detailed knowledge of the state-specific rate coefficients for each reactive and relaxation process. Since such complete information does not exist, it is necessary to consider simplified vibrational schemes. Previous models have considered one effective vibrational level, O_3v (Marinov et al. [27]), or the lowest five [26]. We have developed a scheme comprising six effective vibrationally excited states in addition to the ground state, as shown in Figure 6. Specifically, these are the lowest vibrational bending mode state $O_3(0,1,0)$, a combined stretching mode state $O_3(vc=1)$ ($O_3(1,0,0)+O_3(0,0,1)$) and four effective combined states designated by the effective quantum number vc=v1+v2+v3, $O_3(2\leq vc\leq 5)$, which represent the sum of $O_3(v1,v2,v3)$ states. For clarity, Figure 6, does not show the effective state vc=5, nor the higher-energy states included in the effective combined state $O_3(vc=4)$. We assume that inter-mode vibrational energy transfer collisions of $O_3(vc)$ with O_2 molecules [40, 41] and O atoms [42] ensure near-equilibrium partition inside each effective state $O_3(vc\geq 2)$. Therefore, for each combined vc state, the majority of the population resides in the (lowest energy) bending state $O_3(0,vc,0)$; for example at T_g=293 K, about ~70% of the density of each respective effective state $O_3(vc\geq 2)$ will be in the bending mode, $O_3(0,vc,0)$.

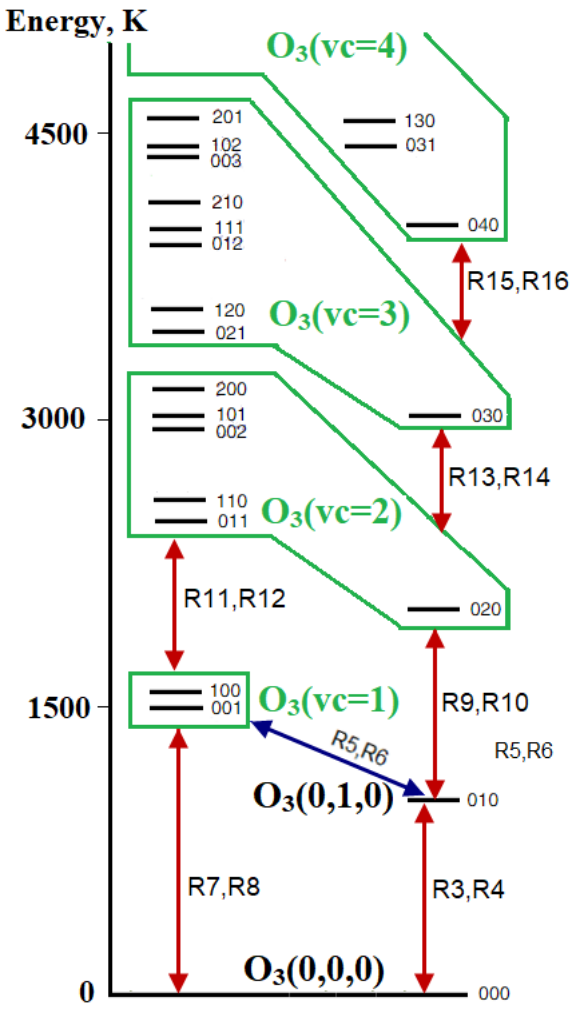

Figure 6. The ozone effective vibrational state scheme used in our model, comprising O_3(0,0,0), O_3(0,1,0), the combined stretching state O_3(vc=1) and the effective combined states O_3(2≤vc≤5) involving various O_3(v1,v2,v3) states with vc=v1+v2+v3. For simplicity, the effective state vc=5 is not shown, and only the three lowest states of O_3(vc=4) are depicted.

The reactions creating vibrationally-excited ozone, the energy transfer processes and the reactions of vibrationally-excited ozone are shown in Table 1, and will be discussed in detail below.

Table 1. Reaction mechanism for ozone vibrational states and rate coefficients of forward (k_d) and reverse (k_r) processes.

N	Reaction	Forward reaction rate: k_d, cm^3/s, cm^6/s	Reverse reaction rate: k_r, cm^3/s
Creation of O_{3v}			
R1	$O(^3P) + 2O_2 \rightarrow O_3(vc\geq1) + O_2$	$5.6\cdot10^{-29}/T_g^2$	
R2	$O(^3P) + O_2 + O(^3P) \rightarrow O_3(vc\geq1) + O(^3P)$	$2.15\cdot10^{-34}\exp(345/T_g)$	
Vibrational energy transfer			
R3	$O_3(010) + O \leftrightarrow O_3(0,0,0) + O$	$2.2\cdot10^{-12}$	$2.2\cdot10^{-12}\exp(-1029/T_g)$
R4	$O_3(010) + O_2 \leftrightarrow O_3(0,0,0) + O_2$	$2.6\cdot10^{-14}$	$2.6\cdot10^{-14}\exp(-1029/T_g)$
R5	$O_3(vc=1) + O \leftrightarrow O_3(0,1,0) + O$	$9.0\cdot10^{-12}$	$1.8\cdot10^{-11}\exp(-560/T_g)$
R6	$O_3(vc=1) + O_2 \leftrightarrow O_3(0,1,0) + O_2$	$2.5\cdot10^{-14}$	$5\cdot10^{-14}\exp(-560/T_g)$
R7	$O_3(vc=1) + O \leftrightarrow O_3(0,0,0) + O$	$4.0\cdot10^{-13}$	$8.0\cdot10^{-13}\exp(-1590/T_g)$
R8	$O_3(vc=1) + O_2 \leftrightarrow O_3(0,0,0) + O_2$	$2.5\cdot10^{-15}$	$5\cdot10^{-15}\exp(-1590/T_g)$
R9	$O_3(vc=2) + O \leftrightarrow O_3(0,1,0) + O$	$1.54\cdot10^{-12}$	$2.2\cdot10^{-12}\exp(-1029/T_g)$
R10	$O_3(vc=2) + O_2 \leftrightarrow O_3(0,1,0) + O_2$	$1.82\cdot10^{-14}$	$2.6\cdot10^{-14}\exp(-1029/T_g)$
R11	$O_3(vc=2) + O \leftrightarrow O_3(vc=1) + O$	$3.08\cdot10^{-12}\exp(-531/T_g)$	$2.2\cdot10^{-12}\exp(-1029/T_g)$
R12	$O_3(vc=2) + O_2 \leftrightarrow O_3(vc=1) + O_2$	$3.64\cdot10^{-14}\exp(-531/T_g)$	$2.6\cdot10^{-14}\exp(-1029/T_g)$
R13	$O_3(vc=3) + O \leftrightarrow O_3(vc=2) + O$	$2.07\cdot10^{-12}$	$2.2\cdot10^{-12}\exp(-1029/T_g)$
R14	$O_3(vc=3) + O_2 \leftrightarrow O_3(vc=2) + O_2$	$2.44\cdot10^{-14}$	$2.6\cdot10^{-14}\exp(-1029/T_g)$
R15	$O_3(vc=4) + O \leftrightarrow O_3(vc=3) + O$	$2.11\cdot10^{-12}$	$2.2\cdot10^{-12}\exp(-1029/T_g)$
R16	$O_3(vc=4) + O_2 \leftrightarrow O_3(vc=3) + O_2$	$2.49\cdot10^{-14}$	$2.6\cdot10^{-14}\exp(-1029/T_g)$
R17	$O_3(vc=5) + O \leftrightarrow O_3(vc=4) + O$	$2.15\cdot10^{-12}$	$2.2\cdot10^{-12}\exp(-1029/T_g)$
R18	$O_3(vc=5) + O_2 \leftrightarrow O_3(vc=4) + O_2$	$2.54\cdot10^{-14}$	$2.6\cdot10^{-14}\exp(-1029/T_g)$
Reactions of O_{3v}			
19a	$O_3(vc) + O \rightarrow 2O_2$	$6\cdot10^{-12}\exp(-E_{19}(vc)/T_g)$	
19b	$O_3(vc) + O \rightarrow O_2(a) + O_2$	$2\cdot10^{-12}\exp(-E_{19}(vc)/T_g)$	
R20	$O_3(vc) + O_2(a) \rightarrow O(^3P) + 2O_2$	$5.2\cdot10^{-11}\exp(-E_{20}(vc)/T_g)$	
R21	$O_3(vc) + O_2(b) \rightarrow O(^3P) + 2O_2$	$1.5\cdot10^{-11}$	
R22	$O_3(0,0,0) + O_2(b) \rightarrow O_3(vc=5) + O_2(a)$	$7.0\cdot10^{-12}$	

4.3.2 Production of vibrationally-excited ozone

The dominant processes of pumping, relaxation and reactive loss of ozone in each state are also shown in figure 6. Vibrationally-excited ozone is mainly produced by the gas-phase three-body reactions:

$$O(^3P) + 2O_2 \rightarrow O_3(vc\geq 1) + O_2 \quad \text{(R1)}$$

$$O(^3P) + O_2 + O(^3P) \rightarrow O_3(vc\geq 1) + O(^3P) \quad \text{(R2)}$$

For these reactions we assumed the total coefficients $k_1=5.6\times10^{-29}/T_g^2$ cm^6/s (from Rawlins et al. [43]) and $k_2=2.15\times10^{-34}\exp(345/T_g)$ cm^6/s (from Baulch et al., [44]). There have been several experimental studies of the nascent vibrational distributions of the ozone product [22, 43, 45, 46]. Von Rosenberg et al. [46] found that (R1) gave an average of 1.6 vibrational quanta in the stretching modes (v1 and v3) and 3.7 quanta in the bending mode (v2). Rawlins and Armstrong [43] observed the infrared emission from vibrationally-excited ozone (up to (0,0,5)) in the reaction of oxygen atoms with oxygen molecules. Considering these observations, along with the results of the photolysis experiments of Azyazov et al [28, 29, 47] we have assumed that both reactions (R1, R2) produce ozone with a distribution across the vc=1-5 states with respective yields of 25, 36, 21, 11 and 7%.

4.3.3 Energy transfer processes in O_{3v}

The vibrationally-excited ozone produced by these reactions is coupled to other vibrational states by collisional V-T transfer processes. The stretching-to-bending inter-mode exchanges (R5,R6): $O_3(vc=1) + M \leftrightarrow O_3(0,1,0) + M$ are shown by a blue arrow in Figure 6, and processes in which the effective vc states are relaxed by one quantum are shown by red arrows.

The rates of VT transfer processes with M = O are generally much faster that the corresponding processes with O_2. Castle et al. [42] measured the rate of (R3), the quenching of $O_3(0,1,0)$ to the vibrational ground state by collisions with O atoms The rate of transfer (R5) between the lowest stretching modes (vc=1) to the bending mode (010) was taken from the measurements of West et al. [21]. For transfers between the higher vc levels (R9, R13, R15, R17) the rates were initially set the same rate as R3, but varied slightly to achieve the best fit to both the experimental observations of Azyazov et al. and to the experimental data in this article. The rate of R7, the quenching of the lowest stretching modes (100) and (001) to the ground state, was initially set to 1/10 of the rate of R5 (following the recommendation of Kaufmann et al. [41] for the analogous processes with O_2 quencher). However, a better fit to our results was obtained using an even smaller value (1/22 of R5). For the reaction R11, the quenching of vc=2 to vc=1 by O atoms, we consider it to be dominated by the loss of one quantum of the bending mode ν_2, i.e. the two processes (110) $\rightarrow$(100)

and (011) → (001). We set the rate to be the same as that for the analogous reaction R9, multiplied by the relative population of these two states relative to (020) (Boltzmann factor) of $2 \cdot \exp(-531/T_g)$, where the factor 2 represents the multiplicity of states. The contribution of the higher states in vc=2 (002, 101 and 200) to the effective rate of the quenching reaction R11 is negligibly small due to the small relative population of these states and the much lower rates of stretching mode VT transfers compared to bending mode transfers.

Now let us consider the rates of VT transfers caused by collisions with O_2. The rates for relaxation of the lowest bending mode, O_3 (010) to the ground state (R4), and for the transfer of the lowest stretching modes to the bending mode, (R6) are based on the measurements of Ménard-Bourcin et al.[48] and Zeninari et al.[49], as discussed by Kaufmann et al. [41]. The direct quenching of the lowest stretching modes to the ground state by O_2 molecules, R8, was set to 1/10 the rate of R6 as recommended by Kaufmann et al. [41]. The rates of transfers between vc states induced by collision with O_2 were initially set to the same rate as the analogous lowest energy process R4, and varied slightly to optimise the fit of our model to the data of Azyazov et al. For the reaction R12, the quenching of vc=2 to vc=1 by O_2 molecules, it is derived from the rate of the analogous R10, using the same logic as used to estimate R11 from R9.

4.3.4 Reactions of O_{3v}

The reactions of ground-state ozone have been well studied [22, 44]. The established value of the rate constant for the reaction with oxygen atoms is $k_{19}(0,0,0) = 8 \cdot 10^{-12} \exp(-2060)/T_g)$ [45], and for the reaction with singlet delta oxygen it is $k_{20}(0,0,0) = 5.2 \cdot 10^{-11} \exp(-2840/T_g)$ [50].

Now let us consider the reactions of vibrationally-excited ozone. Kurylo et al. [20] studied the effect of vibrational excitation in ozone on its reaction with singlet delta oxygen at 298 K. They used an infrared laser to pump the (001) level of ozone, but assumed that the vibrational energy was quickly equilibrated with the other ((100) and (010)) levels. They observed that vibrationally excited ozone reacted significantly faster compared to ground state ozone. If the overall reaction rate increase is attributed only to reactions of the bending mode (0,1,0), then the reaction rate of this level must be enhanced by a factor of 38 ± 20. However, if the stretching modes ((1,0,0) and (0,0,1)) also participate, a rate enhancement of 5-7 is adequate. Hui and Cool [51] observed significant enhancement of the reaction of NO with vibrationally-excited ozone. Rawlins et al. [43] studied the reaction of oxygen atoms with ozone at low temperatures (80-150K) and again found that they are significantly enhanced by vibrational excitation.

Azyazov et al [28, 47] studied the reactions occurring following photolysis of ozone in various gas mixtures. About 50% of the ozone was dissociated, mainly into $O(^1D)$ and $O_2(a)$. This highly non-equilibrium mixture then recombines and reacts, accompanied by the production and

relaxation of vibrationally excited ozone. The time behaviour of O_3 and $O_2(a)$ was measured after the laser pulse (10 ns pulse duration of the used lasers at 248 and 266 nm). The $O(^3P)$ decay was measured in separate experiments in different $O_3/O_2/Ar$ mixtures. They developed a model including vibrational excitation of O_3, and assumed that there was no activation barrier for levels above vc=2. Their model was able to reproduce the temporal behaviour of $O_2(a)$ and the (incomplete) recovery of the O_3 density for certain selected conditions. However, they did not show model results for all gas mixtures.

The decay of the $O_2(a)$, $O_2(b)$ and $O(^3P)$ after the photolysis pulse, and the $O_3(0,0,0)$ recovery are sensitive to the $O_3(vc)$ source distribution in reactions (R1, R2) and the actication barriers of reactions (R19, R20). However, the models of Azyazov and co-workers [28, 29, 47] were unable to reproduce our present measurements of the O_3 density dynamics in a DC discharge afterglow. In general, models using a single effective state of excited O_3 can describe the O_3 afterglow dynamics if the reaction rates are adjusted. However, it was not possible to fit both sets of data (the Azyazov photolysis experiments and the DC afterglow results presented here) using the same set of constants in such a model.

We have assumed that the activation energies, $E_{20}(vc)$, can be expressed in the form $E_{20}(vc)=2840-\alpha \cdot E_{vc}$, where E_{vc}, is the effective energy of the combined vibrational states, and $\alpha \leq 1$ is a vibrational energy efficiency factor [52]. Table 2 summarises the activation energies assumed for the reactions with oxygen atoms, (R19), [45] and with singlet delta oxygen, (R20), [50].

Table 2. Parameters used for the O_3 vibrational states: nascent fractions produced by reactions (R1), (R2), and activation energies for the reactions (R19), (R20).

O_3 vibrational state	Nascent fraction (from R1 and R2)	$E_{19}(vc)/R$ (K) (with O atoms)	$E_{20}(vc)/R$ (K) (with O2a)
(000)	0	2060	2840
(010)	0	1400	1900
vc=1	0.25	1200	1700
vc=2	0.36	900	1300
vc=3	0.21	0	0
vc=4	0.11	0	0
vc=5	0.07	0	0

The rates for the reactions singlet sigma oxygen, $O_2(b)$, with vibrationally-excited ozone (R21) and for its excitation transfer to ground state ozone (R22) were taken from the measurements of Slanger and Black [53].

4.3.5 Validation of our ozone kinetic scheme against photolysis experiments

We tested our ozone vibrational kinetic scheme against the results of the photolysis experiments of Azyazov et al.[47] and of Torbin et al. [29], in which surface loss and production of ozone can be ignored. We were able to reproduce the observed temporal profiles of O_2(a) and O_3(0,0,0), as shown in Figure 7.

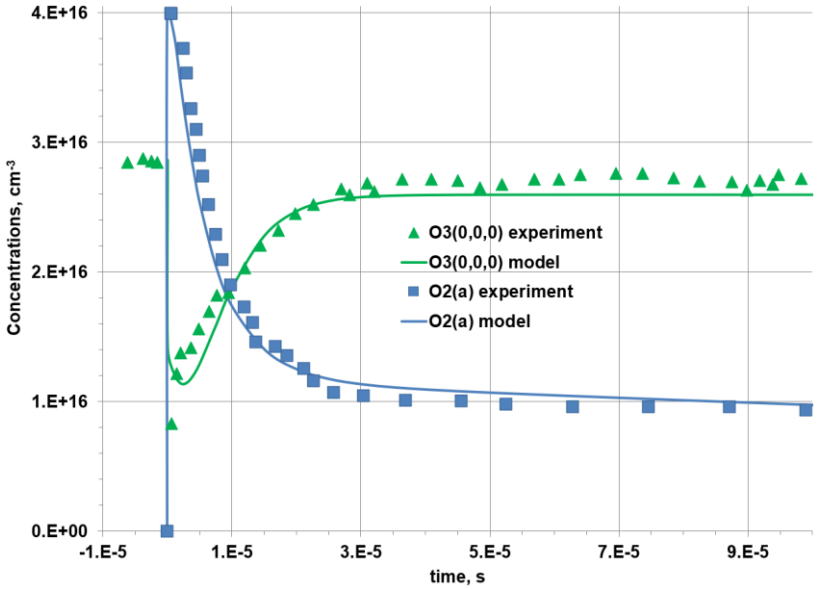

Figure 7. In blue : O_2(a) concentrations after photolysis of ozone (KrF laser at 248 nm) in an O_2/O_3/Ar mixture (partial pressures p_{O2}=680 Torr, p_{Ar} = 90 Torr, p_{O3}=2.4 Torr, laser fluence E = 80 mJ/cm^2, initial gas temperature T = 300 K). The measured data (squares) is from Azyazov et al.[47] and Torbin et al. [29], the results of the present model are shown by solid lines.
In green : O_3(0,0,0) concentrations after photolysis of ozone in an O_2/O_3 mixture, total pressure p=705 Torr, laser fluence E = 70 mJ/cm^2 at 266 nm, initial gas temperature T = 300 K. Measurements from Torbin et al. [29] (triangles) and results of the present model (line).

For the reactions of O_3(vc) with O atoms (R19), the partition between the products O_2 (X) and O_2 (a), as well as the activation energies E_{19}(vc) and E_{20}(vc)), were systematically varied to obtain the best fit to the experimental results (presented here and the photolysis experiments in the literature [28, 29, 47, 54]). A sensitivity analysis [54] performed for the conditions of the photolysis experiment of Azyazov et al. [47] indicated that the O_2(a) decay shows only a weak sensitivity to the partition between reactions 19a and 19b. However, the O_2(a) decay is more sensitive to the rates of the reactions between O_2(a) and O_3(vc), R20. For example, a ~40% reduction of the rate of R20 causes a 20% increase of [O_2(a)] at times after 50 μs.

Azyazov et al. [47] also determined the O(^{3}P) density in their photolysis experiments using titration by NO with detection of the 600 nm luminescence. We simulated these results using our model, with the addition of N_2O, N_2, NO, NO_2, excited NO_2*, and an N/O coupling mechanism. The model showed that the NO_2* emission is not directly proportional to the O(^{3}P) concentration

(as was assumed by Azyazov et al. [47]), due to additional NO_2* emission produced in NO + O_3(vc) → NO_2* + O_2 reactions. The modelled NO_2* behaviour correlates well with the experimental observations when these processes are included. The details and relevance of the titration method used in these photolysis experiments are discussed by Mankelevich et al [54].

5. Discussion

5.1. Comparison of the model to the CRDS results

Now let us compare the results of this new model, which includes ozone vibrational kinetics as well as surface creation and loss of ozone, to the experimental observations. The following parameters are adjusted in the simulations to fit the experimental results: 1) the surface recombination probabilities for O atoms (γ_O^1, γ_O^2) are adjusted to fit the observed steady-state and afterglow densities of oxygen atoms, 2) the ozone surface production parameters ab=0.019, b=0.016, and the surface loss probability, γ_{O3}, are adjusted to fit the afterglow behaviour of O_3, and 3) the surface loss probabilities for O_2(a), γ_{O2a}^1, γ_{O2a}^2, are adjusted to fit the O_2(a) afterglow decays measured in an identical discharge tube presented in Booth et al. [6]. These values, as well as the effective values at the start of the afterglow, $\gamma_{O(t=0)}$ and $\gamma_{O2a(t=0)}$ are presented in Table 3 for the different experimental regimes.

Table 3. The surface loss probabilities (scaled by factor 10^4) for O atoms, O_2(a) and O_3 used in the model.

Regime	p, Torr	γ_O^1	γ_O^2	$\gamma_{O(t=0)}$	γ_{O2a}^1	γ_{O2a}^2	$\gamma_{O2a(t=0)}$	γ_{O3}
1	0.5	3.7	2.9	13.0	6.0	0.7	8.3	0.4
2	1	3.3	1.6	11.3	4.4	0.97	9.3	0.4
3	2	3.2	1.2	11.2	4.4	0.67	8.9	0.32
4	4	3.4	1.1	12.6	3.3	0.83	10.5	0.30
5	4	3.5	1.3	13.8	4.5	0.93	11.9	0.32
6	1	2.7	1.68	9.0	4.1	1.05	8.0	0.38

The calculated near-wall concentrations of O atoms and O_2 at the beginning of the afterglow (i.e. at the end of discharge pulse), and the calculated flux of ozone produced at the surface, FS_{O3} are shown in Table 4. The calculated peak ozone concentrations (O_{3max}) in the discharge afterglow presented in Table 4 and Figures 8-12 will be discussed below. The radial profiles of the O(^{3}P) and O_2(a) concentrations are not uniform during the active discharge, principally because of the significant radial temperature gradient. However, they become

practically uniform after ~5 ms into the afterglow, when the gas temperature $T_g(r)$ has equilibrated to the wall temperature.

Table 4. The calculated concentrations at the beginning of afterglow (at the end of discharge pulse) near the wall, of $[O]_0$, and $[O_2]_0$, the calculated ozone flux created at the surface, FS_{O3} (*ab*=0.019, *b*=0.016) and the peak ozone concentrations (O_{3max}) in the afterglow, for the different discharge regimes studied.

Regime	p, Torr	T_w, K	*I*, mA	$[O]_0$, cm^{-3}	$[O_2]_0$, cm^{-3}	FS_{O3}, $cm^{-2}s^{-1}$	O_{3max}, cm^{-3}
1	0.5	293	40	$3.2\cdot10^{15}$	$1.1\cdot10^{16}$	$2.0\cdot10^{14}$	$2.6\cdot10^{13}$
2	1	293	40	$5.0\cdot10^{15}$	$2.3\cdot10^{16}$	$4.1\cdot10^{14}$	$5.1\cdot10^{13}$
3	2	293	40	$6.8\cdot10^{15}$	$4.6\cdot10^{16}$	$8.0\cdot10^{14}$	$9.2\cdot10^{13}$
4	4	293	40	$8.6\cdot10^{15}$	$9.3\cdot10^{16}$	$1.5\cdot10^{15}$	$1.8\cdot10^{14}$
5	4	283	40	$7.9\cdot10^{15}$	$9.6\cdot10^{16}$	$1.6\cdot10^{15}$	$2.8\cdot10^{14}$
6	1	293	20	$3.8\cdot10^{15}$	$2.6\cdot10^{16}$	$4.4\cdot10^{14}$	$5.8\cdot10^{13}$

The simulation results are compared to the experimental data for all six regimes in Figures 8-12. In these figures the observed linear absorption coefficients are converted to number densities by dividing by the relevant absorption cross-section. In the case of ozone, this molecule is assumed to occupy the entire volume between the CRDS mirrors, and we used a cross-section of $\sigma_{O3}=3.6\times10^{-21}$ cm^2 at 630nm [31, 32], which does not vary significantly with temperature over the range of this study. In the case of oxygen atoms, we assumed that the oxygen density is uniform within the active plasma zone ($0<z<54$cm). In the end-zones there are no electrons and thus no production of oxygen atoms. If the atom density were assumed to be zero in these zones, the density in the active plasma region would be equal to the average density multiplied by the ratio of the optical cavity length to the length of the active plasma zone, i.e. 68/54. A simple diffusion/surface reaction model, using the same surface recombination probability as for the active plasma zone, indicates that the oxygen atom density in the end-zones decays exponentially towards the mirrors, making the effective absorption length longer by 3.6% at 0.5 Torr and by 1.7% at 4 Torr. These small correction factors were taken into account when calculating the oxygen atom densities from the CRDS data. In this case the absorption cross-section at the peak of the transition varies with temperature, both due to the changing Doppler width, and due to the changing distribution across the three spin-orbit levels of the ^3P state (which was assumed to be in equilibrium with the measured atom translational temperature). The temperature-dependent peak

$^3P_2$ cross-section (relative to the total O ^3P_J density) was therefore calculated as described in section 2.

Let us first consider the influence of the vibrational kinetics of ozone on the ozone afterglow dynamics (ignoring, for now, surface loss and production of O_3). The effect of O_3 vibrational kinetics is most pronounced at higher pressures (4 Torr for this study, Figure 8), when surface processes are less significant.

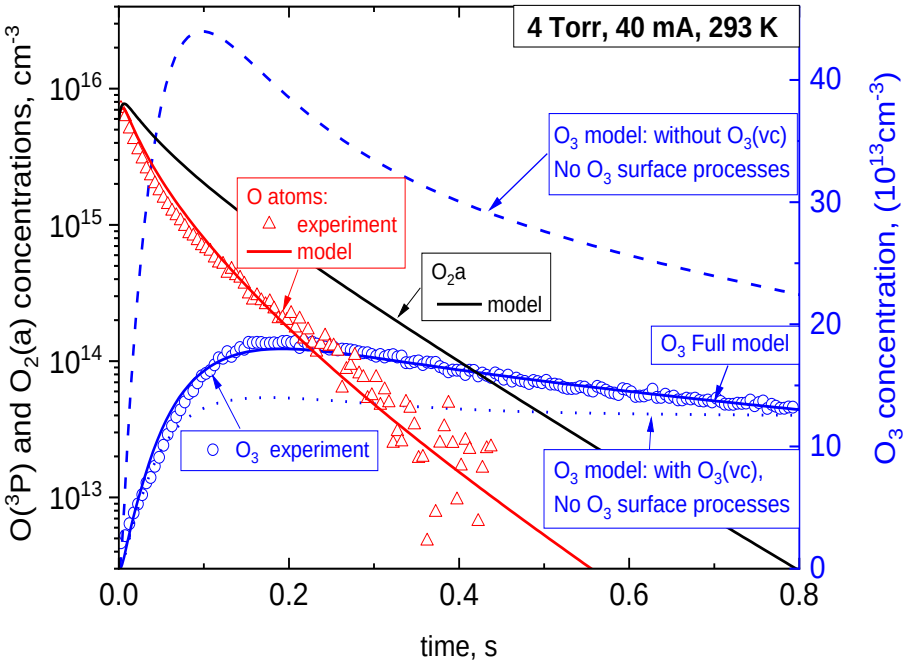

Figure 8. Dynamics of the measured (O_3(0,0,0), O(^{3}P)) and calculated (O_3(0,0,0), O(^{3}P), O_2(a)) axial concentrations in the afterglow of the O_2 discharge at p=4 Torr, I_d=40 mA, T_w=293 K.

At 4 Torr (Figure 8) the model without vibrational kinetics seriously overestimates the ozone concentration (by factor ~2.5), whether or not ozone surface processes are included. In contrast, at 0.5 Torr (Figure 9), models with only gas-phase production of O_3 strongly underestimate the observed ozone densities (whether or not vibrational kinetics is included).

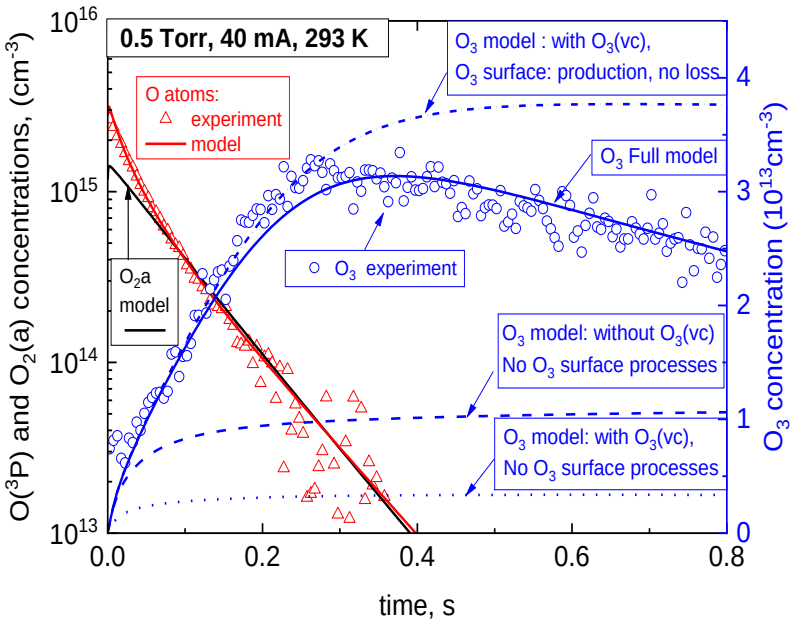

Figure 9. Evolution of the measured (O_3(0,0,0), $O(^3P)$) and calculated (O_3(0,0,0), $O(^3P)$, O_2(a)) axial concentrations in the afterglow of the O_2 discharge at p=0.5 Torr, I_d=40 mA, T_w=293 K.

The excessive ozone density in the model at high pressure can be brought into agreement with the observations by including vibrationally excited states of O_3, and particularly their enhanced destruction by reactions with $O(^3P)$ and O_2(a) in the early afterglow. Simulations including our new O_3 vibrational scheme (but without ozone surface processes) show reasonable agreement with the observed maximal O_3 concentrations at 4 Torr (Figures 8 and 10) although the temporal behaviour is not correct. However, for lower pressure regimes ($p \leq 2$ Torr, Figures 9, 11,12), models without surface ozone processes seriously underestimate the ozone density.

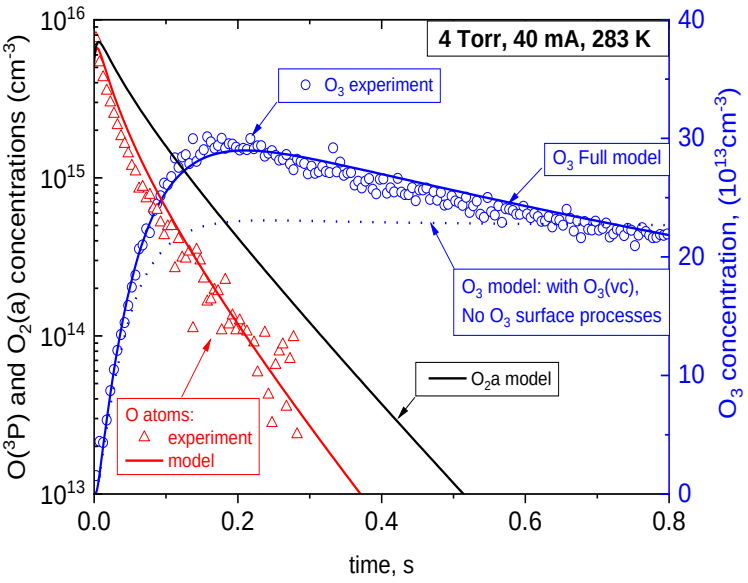

Figure 10. Evolution of the measured (O_3(0,0,0), $O(^3P)$) and calculated (O_3(0,0,0), $O(^3P)$, O_2(a)) axial concentrations in the afterglow of the O_2 discharge at p=4 Torr, I_d=40 mA, T_w=283 C.

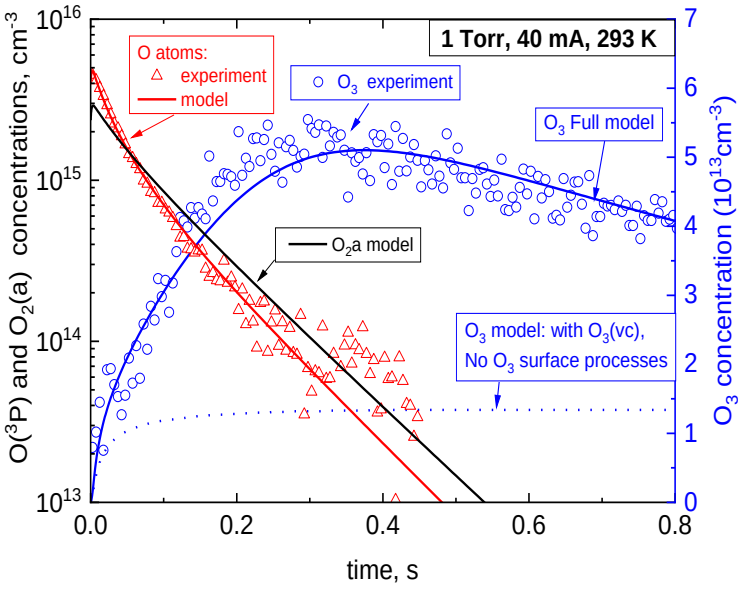

Figure 11. Evolution of the measured (O_3(0,0,0), $O(^3P)$) and calculated (O_3(0,0,0), $O(^3P)$, O_2(a)) axial concentrations in the afterglow of the O_2 discharge at p=1 Torr, I_d=40 mA, T_w=293 K.

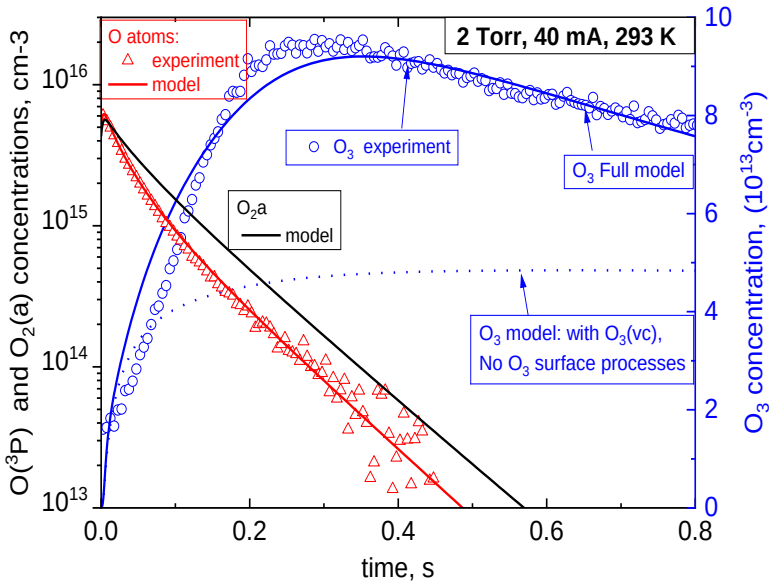

Figure 12. Evolution of the measured (O_3(0,0,0), $O(^3P)$) and calculated (O_3(0,0,0), $O(^3P)$, O_2(a)) axial concentrations in the afterglow of the O_2 discharge at p=2 Torr, I_d=40 mA, T_w=293 K.

The observed ozone density at lower pressures is seriously underestimated without the inclusion of O_3 surface production. The simulation for p=0.5 Torr, including both O_3 vibrational kinetics and the O_3 surface source FS_{O3} (proportional to O_2 flux from Table 4 -see also Section 5.3), is shown in Figure 9. Note that the excellent agreement of the modelled oxygen atom dynamics to the observations is only the consequence of the oxygen surface recombination coefficients (γ_O^1 and γ_O^2) being adjusted in the model to fit the experimental data. These results were obtained using the assumption that all ozone produced at the surface is in the O_3(vc=2) level. We also tested models in which the surface-produced ozone is distributed over the O_3(vc=1,2,3) levels (and with different total yields compared to the simple case), but they all produce broadly similar results. However, any ozone produced in levels higher than (vc>3) produces negligible amounts of ground-state ozone: this is because highly-excited ozone is lost very quickly by reactions with O (R19), O_2(a) (R20), O_2(b) (R21), before it can be relaxed to the ground state.

The relative contribution of surface ozone production is much smaller at higher pressure (*e.g.*, at p=4 Torr, Figure 8 and 10). Gas-phase production of O_3 in three-body reactions becomes dominant due to the near cubic pressure dependence of the gas-phase sources compared to the linear pressure dependence of surface production.

Even though there is no direct creation of vibrational ground state ozone (either at the surface or by the three-body reactions R1 and R2), the modelled concentrations of vibrationally excited O_3(vc≥1) are always more than order of magnitude lower that of ground state ozone under all conditions, due to the fast V-T relaxation by both O and O_2 (see Section 5.2 for details).

We also tested a model where the surface production of O_3 is assumed to be proportional to the incident flux of O atoms (rather than O_2 molecules). We assumed that ~5% of the lost flux of O atoms is converted into ozone. At the lowest pressure of 0.5 Torr this model was able to reproduce the peak ozone density, O_{3max}, but gives a totally different temporal behaviour; the ozone peak is reached much too fast, because the oxygen atom flux to the surface decays quickly in the afterglow, causing this source term to stop: the maximum is reached at t~0.1 s in this model, compared to the observed peak time of t~0.25-0.45 s (Figure 9). This discrepancy could not be resolved by changing either the amplitude of this process or the effective vibrational level (vc) of the produced O_3.

Under all conditions, after reaching a peak density (O_{3max}) after a few hundred milliseconds, the ozone density decays slowly in the late afterglow. At this time the O and O_2(a) concentrations are very low, therefore gas-phase reactions with these species cannot be responsible for this observed ozone decay. This decay can only be attributed to surface destruction (in addition to a small contribution from transport by gas flow). This decay in O_3 density at long times was reproduced in the model by adding an O_3 surface loss term, γ_O_3, defined in Table 3. This parameter decreases with pressure, from $0.5x10^{-4}$ at 0.5 Torr to $0.3x10^{-4}$ at 4 Torr

The results of the simulation including ozone vibrational kinetics, surface creation, and surface loss are shown in Figures 8-12 (blue lines for $[O_3](t)$ and red lines for $[O(^3P)](t)$). Good agreement is seen with the observed $[O_3](t)$ (blue symbols) and [O](t) (red symbols) for all regimes under study. The relative contribution of surface production to the total O_3 production (and thus the ozone maxima (O_{3max})) decreases progressively with pressure, from ~90% (at 0.5 Torr), ~75% (at 1 Torr), (Figures 9 and 11), to about ~20% at 4 Torr (Figures 8 and 10).

Although production of ozone in the gas phase and at the surfaces also occurs during the active discharge, any ozone produced is quickly destroyed by electron impact, thermal dissociation and reactions R19-R21. As a result, the ozone density is negligible during the active discharge, in both ground and vibrationally excited states. The model predicts ground-state ozone densities during the discharge of $[O_3(0,0,0)](r=0) = 3.8\times10^{11}$, 4.5×10^{11}, 5.4×10^{11}, 6.7×10^{11}, 6.8×10^{11} and 5.3×10^{11} cm^{-3} for regimes 1-6, respectively. These values are much lower than the corresponding values of O_{3max} in the afterglows. The density of vibrationally excited ozone is more than an order of magnitude lower than that of the ground state in the active discharge. As a result, ozone and its kinetics have little effect on the calculated concentrations of $O(^3P)$, O_2(a) and other species in the active discharge.

The CRDS measurements (Section 3) indicate the presence of some ozone density during the active discharge and at the beginning of the afterglow. As discussed above, this can be attributed to the accumulation of ozone in the regions between the active discharge glow and the

CRDS mirrors (the “end-zones”). We were able to model this using a 2-D(r,z) model involving the derived ozone surface source (these modelling results will be reported elsewhere). However, this ozone present at the beginning of the afterglow is small compared to that occurring in the afterglow. This does not significantly change the model results: the simulated O_3 density produced in the afterglow hardly depend on the initial O_3(t=0) density value over a fairly wide range.

5.2. Evolution of ozone vibrational distribution in the afterglow.

The model shows that all vibrationally excited states (but especially the lower states, O_3(vc=1,2) and O_3(0,1,0)) contribute to the loss of total ozone through the reactions (R19, R20) with rates comparable to that of ground state ozone. The calculated densities of ozone in the afterglow in different vibrational states are presented in figure 13 for discharge regime 4 (4 Torr, 40 mA, 20 C). In the early afterglow, the higher vibrational states are overpopulated, due to their direct production by the three-body recombination reactions (R1, R2). The fast exothermic reaction of ozone (in all vibrational states) with O_2(b) (R21) [45] causes significant ozone destruction at the very start of the afterglow(t<20 ms), but this process quickly disappears due to the fast decay of O_2(b). As the concentrations of O(^{3}P), O_2(a) and O_2(b) decrease (and therefore the rates of the ozone loss/production processes (R1, R2, R19, R20, R21)) the O_3 vibrational distribution approaches thermal equilibrium (at the respective gas temperature T_g~T_w). This happens more quickly for the lower vibrational states, followed by the higher states. Inside each effective combined vibrational state, O_3(vc), the equilibrium fractions of the lowest bending state O_3(0,vc,0) and stretching states O_3(1,vc-1,0)/O_3(0,vc-1,1) at T_g=293 K are ~70% and ~23%, respectively, corresponding to the Boltzmann distribution inside the effective state O_3(vc). The ratio of the equilibrium concentrations [O_3(vc+1)]/[O_3(vc)] should be about ~0.03 for vc=2-4 from the energy difference given in the energy diagram in Figure 6. Figure 13 shows that these ratios are reached in the late afterglow for vc=2 but not for vc≥3. The low concentrations of vibrational states with vc≥3 (Figure 13) is a result of their faster loss by reactions 19 and 20, which have no activation energy barrier.

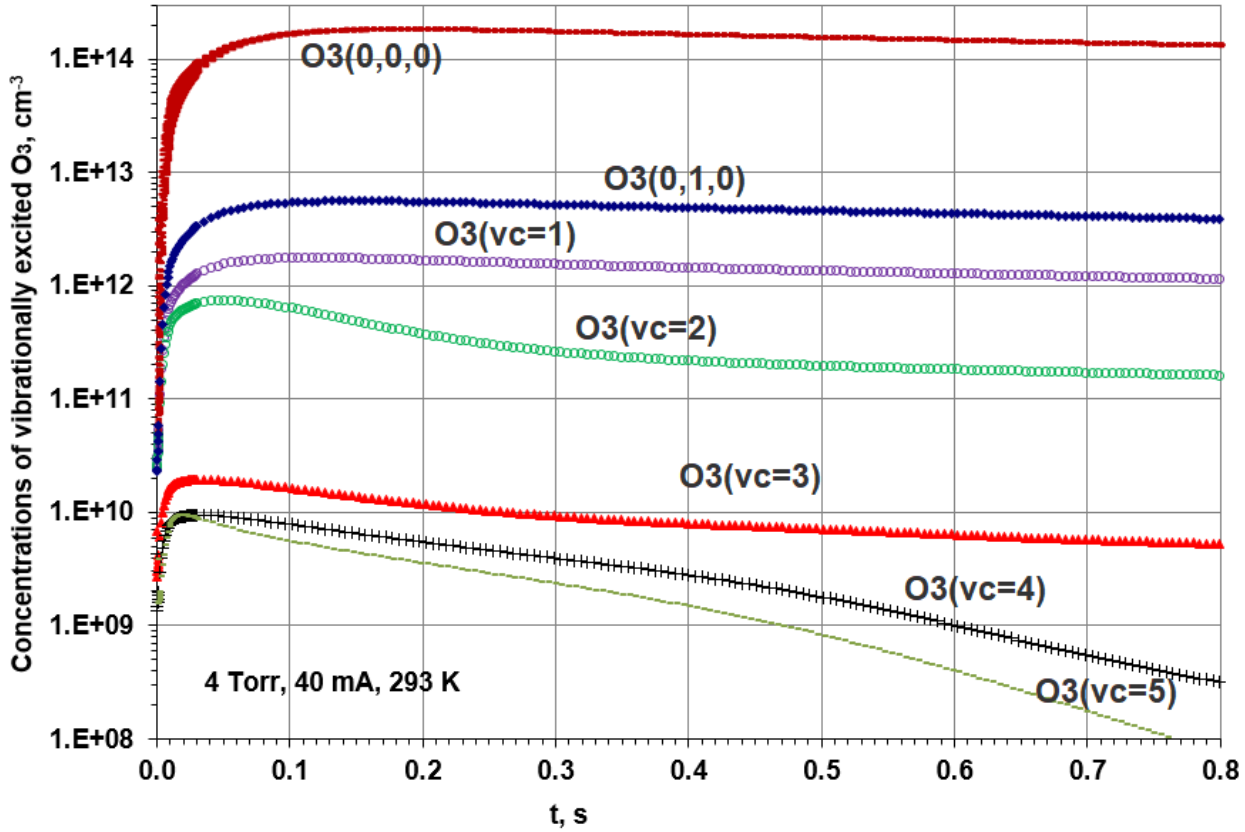

Figure 13. The calculated evolution of axial concentrations of O_3(0,0,0) and the vibrationally excited ozone molecules in the afterglow of the O_2 discharge at p=4 Torr, I_d=40 mA, T_w=293 C.

5.3. O_3 surface production mechanism.

The observed dynamics of O_3 in the afterglow at low pressure can only be explained by an O_3 surface source proportional to the incident O_2 flux. However, this surface production of O_3 must be coupled with the O surface loss mechanism. The simplest model (neglecting reactions involving O_2(a) and O_2(b), which would require a separate study) involves incident O atoms, O_2 and O_3 molecules and various categories of surface sites, i, involving free surface sites S*(i) and respective $O_{ad}S(i)$ sites (O atoms adsorbed on S*(i) with adsorption energy $E^i_{ad}(O_{ad}S(i))$). Each type of surface site has a specific adsorption energy, E^i_{ad}, and surface density $[S_0(i)] = [S^*(i)] + [O_{ad}S(i)]$. The sum of these concentrations $\Sigma[S_0(i)]$ should be equal to or lower than total surface site concentration $[S_t]$ which is specific to the surface conditions. Cartry et al. [55] assumed a total surface site density for fused silica of $[S_t]=2.5\times10^{15}$ cm^{-2}. Other studies of crystalline and amorphous silica [56, 57] found surface silicon atom densities of ~ 5×10^{14} cm^{-2}. The surface site density on a borosilicate glass surface is less well known.

Let us first consider a simplified model, comprising a single type of surface site (i.e. omitting the index i) with one reaction mechanism and with an adsorption energy in the range $0.6\leq E_{ad}\leq1$ eV relevant for the O_3(vc≤3) production. These sites can participate in adsorption (2), thermal desorption (2, reverse reaction), O atom recombination (3), and ozone production (4):

$$O + S^* \leftrightarrow O_{ad}S \quad (2)$$

$$O + O_{ad}S \rightarrow O_2 + S^* \quad (3)$$

$$O_2 + O_{ad}S \rightarrow O_3(vc) + S^* \quad (4)$$

The fluxes of O and O_2 to the surface will determine the fraction of occupied surface sites in the quasi-steady state balance $(k_3[O] + k_{-2} + k_4[O_2])[O_{ad}S] = k_2[O]([S_0] - [O_{ad}S])$, leading to the following expression for $[O_{ad}S]$ as a function of the concentrations [O] and $[O_2]$ near the tube surface:

$$[O_{ad}S] = k_2[S_0]/(k_3 + k_2 + (k_{-2} + k_4[O_2])/[O]) \quad (5)$$

The flux of ozone produced by the surface FS_{O3} (in $cm^{-2}s^{-1}$), is then given by:

$$FS_{O3} = k_4[O_2][O_{ad}S] \quad (6)$$

The rate constant of the reaction (2) is expected to be quite high for radical addition to a radical site. We express the rate of thermal desorption, k_{-2}, in an Arrhenius form: $k_{-2} = \nu_d \times \exp(-E_{ad}/T_w)$. The pre-exponential factor ν_d is assumed to be $\sim 5\times10^{13}$ [58]. It is known from transition state theory for gas phase dissosiation reactions and from experimental data [59] that the effective vibrational frequency of molecules is about $\sim 10^{13}$ s^{-1}. An extension of this approach to describe the pre-exponential factor for desorption from surfaces, without taking into account collisions between gaseous particles and the surface, appears quite resonable (excluding metals [60]). The inclusion of these collisions can increase the pre-exponential factor up to 10^{15} s^{-1}.

For T_w=293 K and E_{ad}=0.8 eV we get $k_{-2} < 0.8$ s^{-1}, which is small, indicating that the term k_{-2} can be neglected in equation (5) for most conditions. In this case, combining (4) and (5) gives the flux of ozone produced at the surface to be:

$$FS_{O3} = ab[O_2]/(1+b[O_2]/[O]) \quad (7)$$

as a function of the near-wall concentrations $[O_2]$, [O], with the parameters $a=k_2[S_0]$ and $b=k_4/(k_3+k_2)$.

This model for surface production of ozone, with two adjustable parameters *a* and *b*, was incorporated into the model as described above. These parameters were systematically varied to establish the optimal (relative to $[O_3]_{max}$ value and time position) product $ab \sim 0.019\pm0.002$ and best values $a \approx 1.2$ cm/s and $b \approx 0.016$ for all regimes under study. In the early afterglow, we have $b[O_2]/[O] << 1$, so that the ozone production is independent of the incident O atom flux. The surface concentration $[O_{ad}S] \approx k_2[S_0]/(k_3+k_2)$ is then almost constant, and $FS_{O3} \approx 0.019\times[O_2]$ $cm^{-2}s^{-1}$. The second term, $b[O_2]/[O]$ in (7), becomes significant at low concentration ratios $[O]/[O_2]$, resulting in reduced ozone production, FS_{O3} (*e.g.*, by factor ~2 at $[O]/[O_2]\sim0.016$ reached at the end of the initial linear growth of $[O_3](t)$ which is seen in Figures 8-12). The values of the parameters *a* and *b* used here can be the result of different combinations of k_2, k_3, k_4 and $[S_0]$. The

temperature dependence of these rate coefficients, and effects of the previous conditioning of the tube surface will be discussed in a separate paper.

This reaction mechanism could also be affected by exothermic reactions of $O_2(a)$ molecules, which could remove oxygen atoms from the surface through the production of unstable electronically excited ozone O_3^* , which will then dissociate into $O_2 + O$, having the overall effect of:

$$O_2(a) + O_{ad}S \rightarrow O_2 + O + S^* \quad (8)$$

In this case, the parameter b becomes $b=k_4/(k_3+k_2+k_8[O_2(a)]/[O])$. We could then obtain similar results for the ozone dynamics using the same value of $a\approx1.2$, and ratio $k_4/(k_3+k_2+k_8) \approx 0.016$. In this case, and in conditions of $[O_2(a)]/[O]\sim1$, the new parameter b would be close to previous $b=k_4/(k_3+k_2)$. Therefore, our experimental results cannot confirm or disprove any contribution of reaction (8). This, and other surface reactions of $O_2(a)$ require additional study.

5.4. Surface destruction of ozone

In the late afterglow, the concentrations of O, $O_2(a)$ and other active species are much lower than that of O_3, so the mixture consists principally of O_3 in O_2. The observed decays of O_3 in the far afterglow at different pressures were dependent on the wall temperature. This implies that the O_3 surface loss mechanism is temperature-dependent, and does not depend on an incident flux of O atoms or other active species. To meet these requirements, we can propose the following simple cyclic mechanism for O_3 surface destruction:

$$O_3 + S^* \rightarrow O_2 + O_{ad}S \quad (9)$$

$$O_3 + O_{ad}S \rightarrow 2O_2 + S^* \quad (10)$$

Sites with oxygen atom having an adsorption energy of $E_{ad} > 0.6$ eV could be involved in this surface loss of ozone. For incident $O_3(0,0,0)$ molecules, reaction (9) will be endothermic if the adsorption energy is below 1 eV. It is also possible that there are energy barriers for reactions (9) and (10), dependent on both E_{ad} and the vibrational state of O_3 , which would require a separate study.

The possibility of such a cyclic mechanism of ozone surface destruction is discussed by Mazankova et al. [39] for alumina and copper surfaces previously treated by ozone. Mankelevich et al. [7] studied ozone loss on Al_2O_3 surfaces, and suggested a mechanism consisting of the formation of a layer of chemisorbed O_3 (attached to surface Al atoms) followed by O_3 phyisorption (O_{3phys}) and further reactions of O_{3phys} with incident ozone molecules.

The observed decay of the ozone density in far afterglow (Figures 8-12) can be reproduced in the model using the surface loss probabilities given in Table 3. Additional experimental results at p=4 Torr with a higher wall temperature T_w=323 K (+50°C) show a faster ozone decay rate in

the far afterglow, which can be reproduced in the model using a larger value of γ_{O3}(p=4 Torr, T_w=323 K) = 4.3×10^{-5}. The values of γ_{O3} obtained as a function of pressure and temperature allows the O_3 surface loss probability to be expressed in an Arrhenius form: $\gamma_{O3}(\text{surf}, T_w) \sim 0.002\times\exp(-E_{act}/T_w)$ with an activation energy $E_{act} \sim 1350$ K. A slightly faster increase of $\gamma_{O3}(T_w)$ with temperature was observed by Itoh et al. [61] on Pyrex surfaces. Separate experiments were made at MSU using a surface wave discharge in O_2 at 1 Torr to estimate the ozone surface loss probability γ_{O3} in a quartz tube. The tube was first treated for tens of minutes, and then filled with an O_3/O_2 mixture, and the O_3 decay was observed at room temperature by ozone UV absorption. The values of γ_{O3} obtained were in a very similar range: $\gamma_{O3} \sim (1\text{-}2)\cdot10^{-5}$.

5.5. Maximal O_3 concentrations in the afterglow as a function of discharge parameters

5.5.1 Pressure dependence of O_{3max}. The maximal O_3 concentrations predicted by a model without any ozone surface processes show near quadratic dependence on the pressure (see Figures 8, 9, 11, 12 (open circles)). This is to be expected from the near cubic ($\sim p^3$) pressure dependence of the main O_3 source (reaction (R1)) balanced by the near linear pressure dependence of the O_3 loss frequency (reactions (R19, R20). When the surface source of O_3 is included (which is most significant at low pressures $p\leq1$ Torr), the calculated pressure dependence of O_{3max} becomes close to linear (Table 4, regimes 1-4). This corresponds well with the observed O_{3max}(CRDS) (Figures 8, 9, 11, 12 solid diamonds).

5.5.2 Wall temperature dependence of O_{3max}.

A later set of measurements were made with the wall temperature set to 10, 20 and 50C. These measurements were made in the same discharge tube, but taken many months later. In these experiments the surface recombination of oxygen atoms was clearly faster, leading to lower steady-state atom densities and faster atom decay rates in the afterglow. Figure 14 shows how the O_3 afterglow dynamics depend on the wall temperature (10, 20 and 50°C) at pressures of 0.5 Torr (figure 14a) and 4 Torr (figures 14b). The maximal ozone density, O_{3max}, is significantly reduced when the wall temperature is increased to +50°C. The difference (20°C to 50°C) is bigger at 4 Torr (a factor of 2.7 in the experimental data and 2.9 in the model) compared to 0.5 Torr (a factor of 1.7 in both the experimental data and the model results).

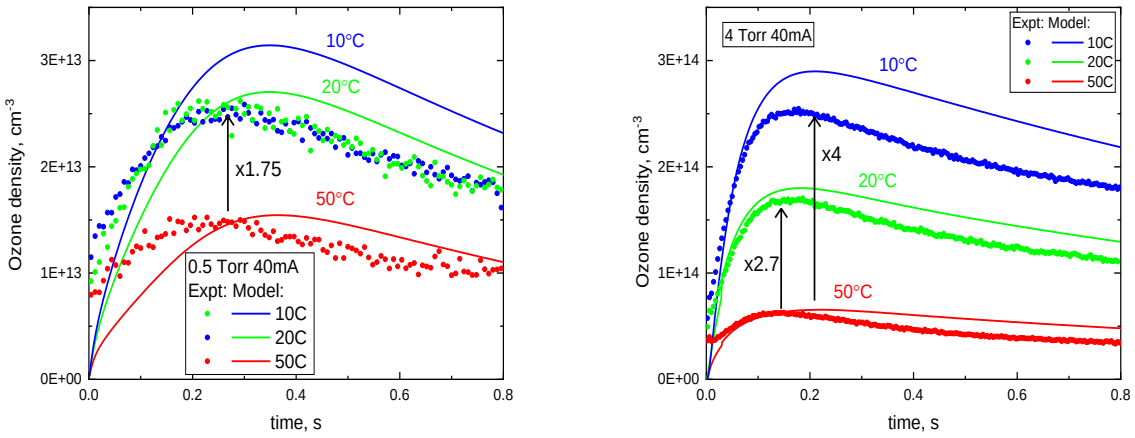

Figure 14. O_3 afterglow dynamics as a function of wall temperature at pressure values of (a) 0.5 Torr and (b) and 4 Torr. Experimental measurements are shown as dots, model results as lines.

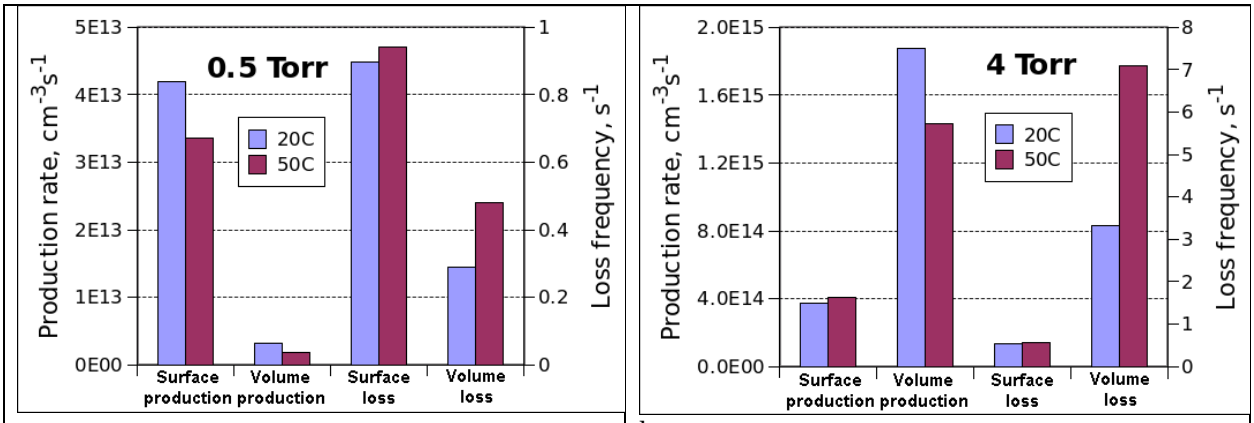

Figure 15. O_3 volume and surface production rates and loss frequencies for pressure values of 0.5 Torr (a) and 4 Torr (b) and for T_w values of 20 and 50 °C. The time value t corresponds to the maximum of $[O_3]$.

This higher $O_{3max}(T_w)$ at lower wall temperatures can be explained by the changes in the balance of production and loss reactions. For the ozone production/loss balance we use simple estimations for the reaction with ground state $O_3(0,0,0)$. Figure 15 shows the O_3 volume (R1, R2) and surface production (FS_{O3}) rates and volume (R19+R20) and surface loss frequencies for pressure values of 0.5 Torr (Figure 15a) and 4 Torr (Figure 15b) for T_w values of 20 and 50° C at the time in the afterglow when $[O_3]$ reaches its maximum value.

For the highest pressure regime studied (4 Torr), gas phase processes loss and production of ozone dominate over surface processes. The production of ozone is proportional to the pressure cubed, p^3 while surface ozone production is linear with pressure, therefore the ratio of volume to surface ozone production is proportional to p^2 Thus at even higher pressures the contribution of

surface processes will become increasingly negligible. In the afterglow the gas temperature quickly relaxes to the wall temperature. The increase of $O_{3max}(T_w)$ at lower wall temperatures can be explained by the decrease in the rate of the gas-phase ozone reactions with O atoms (R19) and with $O_2(a)$ (R20) with a simultaneous increase in the three-body production process, (R1).

The gas phase loss rate of O_3 at 293 K in reactions R20 and R19 (ν_{20}=2.1 s^{-1}, ν_{19}=1.2 s^{-1}) is lower than corresponding losses at 323 K (ν_{20}=4.5 s^{-1}, ν_{19}=2.6 s^{-1}) by a factor of 2.2. At the same time, the rate of main ozone source reaction, $R_1=k_1[O][O_2]^2$ increases by about 30% for a T_g drop from 323 to 293 K, due to the increase of both the rate coefficient $k_1 \sim T_g^{-2}$ and the O_2 concentration $[O_2] \sim N \sim 1/T_g$ (N is total gas concentration). This results in a ~ 2.9 times difference in O_3max for 4 Torr pressure, which is shown in Figures 14c and 14d both in the model and experiment.

For the lower pressure regime of 0.5 Torr the surface processes must be taken into consideration, both for the ozone production and loss. Ozone production at this pressure is determined by the surface source, $FS_{O3}(7)$, which is much higher than volume production by (R1). The O_3 production is about 1.2 times higher at 293 K, due to changes of both $[O_2]$ and $[O_2]/[O]$. The ozone loss rate at the wall (ν_{wall} is about 1 s^{-1}) is faster than volume loss (ν_{20}=0.2 s^{-1}, ν_{19}=0.1 s^{-1} at 293 K and ν_{20}=0.3 s^{-1}, ν_{19}=0.2 s^{-1} at 293 K), so the relative decrease in the loss rate is also lower. As a result, the lower relative difference in O_3max value at lower pressure with the same change in T_{wall} value is the result of ozone surface production and loss processes.

5.5.3 Current dependence of O_{3max}.

The variation of the ozone density in the afterglow for 20 and 40 mA at pressures of 0.5 and 4 Torr are shown ion figure 16. Both experimental measurements (dots) and model results (lines) are shown. At a given pressure the current has little effect on the afterglow ozone density, the principal difference being a slightly higher ozone density at the start of the afterglow in the case of 0.5 Torr, indicating a higher build-up of ozone in the dead zones due to the higher steady-state oxygen atom density. The quantity of ozone created in the afterglow shows no significant dependence on the current, as would be expected from the surface production of ozone from the reaction of O_2 molecules with a surface saturated on oxygen atoms, as discussed above. The main effect of the discharge current is on steady state (and therefore at the start of the afterglow) values of [O], $[O_2(a)]$, and the gas temperature. However these values fall rapidly at the start of the afterglow, reaching similar values for both regimes (with relaxation times t_r < 10 ms for $T_g(t)$, t_r < 50 ms for [O](t) and t_r < 100 ms for $[O_2(a)](t)$). This results in a weak dependence on discharge current, which correlates with the O and $O_2(a)$ number densities.

In figure 16, the model predicts a slightly lower value of O_{3max} at 40 mA compared to 20 mA case, due to higher [O] and $[O_2(a)]$, which is not seen in the experimental results. Also, each simulation

is adjusted to the specific tube conditions by varying the surface loss coefficients to describe the experimentally measured stationary density and afterglow dynamics of O atoms.

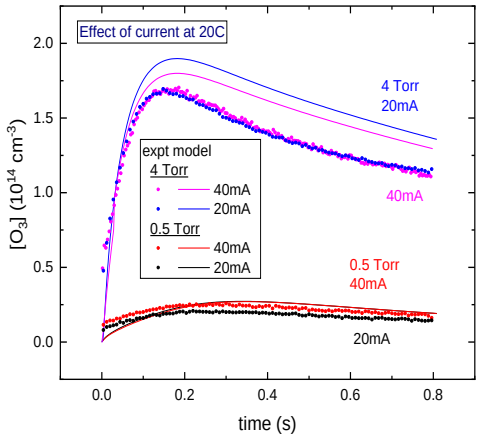

Figure 16 Ozone densities in the afterglow at 0.5 and 4 Torr, 20°C, for currents of 20 and 40 mA. The experimental data is shown as dots, the model as full lines

6. Conclusions

Time-resolved cavity ringdown spectroscopy measurements at 630 nm have been used to probe the kinetics of O atoms and O_3 molecules in O_2 dc discharges and their afterglows over a range of discharge currents, gas pressures and borosilicate glass tube temperatures. In the afterglow, the oxygen atom density decays non-exponentially, indicating a surface loss process with linear and quadratic terms. Significant ozone densities build up in the afterglow, peaking after a few hundred milliseconds. The observed maximal $O_3(0,0,0)$ concentrations (O_{3max}) dramatically increase with increasing pressure and with lowering tube temperature, but vary little with the discharge current. Most of the experimental results and trends are well explained by a 1D radial model, both for the steady-state positive column O_2 discharge and the afterglow plasma decay. For this it was necessary to add the kinetics of vibrationally-excited ozone and ozone surface loss/production reactions. It was shown that the measured non-exponential decay of O atoms in early afterglows is related to a changing O atom surface loss probability (e.g. dependent on the O atom concentration near the tube surface). The same surface reaction is able to reproduce the time-resolved behaviour $O(^3P)$ and O_3 for all discharge regimes studied here. The necessity to include O_3 surface production (in reactions of the incident O_2 molecules with the adsorbed O atoms) and surface-temperature-dependent loss (with probabilities of the order 10^{-5}) is discussed.

Acknowledgments

The authors from Lomonosov MSU are grateful to the Russian Scientific Foundation (RSF), project no. 21-72-10040, for supporting this study. The LPP team recieved financial support from the Fédération de Recherche PLAS@PAR.

References

[1] Hook D A, Olhausen J A, Krim J and Dugger M T *Journal of Microelectromechanical Systems* 2010 **19** 1292-1298
[2] Singh M K, Ogino A and Nagatsu M *New Journal of Physics* 2009 **11** 115027
[3] Takeuchi N and Yasuoka K *Japanese Journal of Applied Physics* 2020 **60** SA0801
[4] Yang W and Wolden C A *Thin Solid Films* 2006 **515** 1708-1713
[5] West A, van der Schans M, Xu C, Cooke M and Wagenaars E *Plasma Sources Science and Technology* 2016 **25** 02LT01
[6] Booth J P, Chatterjee A, Guaitella O, Sousa J S, Lopaev D, Zyryanov S, Rakhimova T, Voloshin D, Mankelevich Y, de Oliveira N and Nahon L *Plasma Sources Science and Technology* 2020 **29** 115009
[7] Mankelevich Y A, Voronina E N, Poroykov A Y, Rakhimov T V, Voloshin D G and Chukalovsky A A *Plasma Physics Reports* 2016 **42** 956-969
[8] Mitchell A C G and Zemansky M W *Resonance Radiation and Excited Atoms*. Cambridge: Cambridge University Press, 2009
[9] Booth J P, Joubert O, Pelletier J and Sadeghi N *Journal of Applied Physics* 1991 **69** 618-626
[10] Nagai H, Hiramatsu M, Hori M and Goto T *Review of Scientific Instruments* 2003 **74** 3453-3459
[11] Niemi K, O'Connell D, de Oliveira N, Joyeux D, Nahon L, Booth J P and Gans T *Applied Physics Letters* 2013 **103**
[12] Czerwiec T, Gavillet J, Belmonte T, Michel H and Ricard A *Surface and Coatings Technology* 1998 **98** 1411-1415
[13] Lopaev D V, Volynets A V, Zyryanov S M, Zotovich A I and Rakhimov A T *Journal of Physics D: Applied Physics* 2017 **50** 075202
[14] Goehlich A, Kawetzki T and Döbele H F *The Journal of Chemical Physics* 1998 **108** 9362-9370
[15] Peverall R, Rogers S D A and Ritchie G A D *Plasma Sources Science and Technology* 2020 **29** 045004
[16] Booth J P, Chatterjee A, Guaitella O, Lopaev D, Zyryanov S, Volynets A, Rakhimova T, Voloshin D, Chukalovsky A, Mankelevich Y and Guerra V *Plasma Sources Sci. Technol.* 2022 **31** 065012
[17] Booth J P, Guaitella O, Chatterjee A, Drag C, Guerra V, Lopaev D, Zyryanov S, Rakhimova T, Voloshin D and Mankelevich Y *Plasma Sources Science and Technology* 2019 **28** 055005
[18] von Rosenberg C W and Trainor D W *The Journal of Chemical Physics* 1973 **59** 2142-2142
[19] Lin C and Leu M *International Journal of Chemical Kinetics* 1982 **14** 417-434
[20] Kurylo M J, Braun W, Kaldor A, Freund S M and Wayne R P *Journal of Photochemistry* 1974 **3** 71-87
[21] West G A, Weston R E and Flynn G W *Chemical Physics Letters* 1976 **42** 488-493
[22] Rawlins W T, Caledonia G E and Armstrong R A *The Journal of Chemical Physics* 1987 **87** 5209-5221

[23] Klopovskii K S, Kovalev A S, Lopaev D V, Rakhimov A T and Rakhimova T V *Soviet Journal of Plasma Physics* 1992 **18** 834-839
[24] Klopovskii K, Kovalev A, Lopaev D, Popov N, Rakhimov A and Rakhimova T *Journal of Experimental and Theoretical Physics - J EXP THEOR PHYS* 1995 **80** 603-613
[25] Vlasov M, Klopovsky K, Lopaev D, Popov N, Rakhimov A and Rakhimova T *Cosmic Research* 1997 **35** 219-225
[26] Lopaev D V, Malykhin E M and Zyryanov S M *Journal of Physics D: Applied Physics* 2011 **44** 015202
[27] Marinov D, Guerra V, Guaitella O, Booth J-P and Rousseau A *Plasma Sources Science and Technology* 2013 **22** 055018
[28] Azyazov V N and Heaven M C *International Journal of Chemical Kinetics* 2014 **47** 93-103
[29] Torbin A P, Pershin A A and Azyazov V N *Izvestiya Samarskogo nauchnogo tsentra RAN (Proceedings of the Samara Scientific Center of the Russian Academy of Sciences)* 2014 **16** 17-21
[30] Kramida A, Ralchenko Y, Reader J and NIST-ASD-Team-(2022) "NIST Atomic Spectra Database (ver. 5.10), [Online]. Available: https://physics.nist.gov/asd [2023, February 15]. " 2022.
[31] Serdyuchenko A, Gorshelev V, Weber M, Chehade W and Burrows J P *Atmospheric Measurement Techniques* 2014 **7** 625-636
[32] Orphal J *Journal of Photochemistry and Photobiology A: Chemistry* 2003 **157** 185-209
[33] Branscomb L M, Burch D S, Smith S J and Geltman S *Physical Review* 1958 **111** 504-513
[34] Belostotsky S G, Economou D J, Lopaev D V and Rakhimova T V *Plasma Sources Science and Technology* 2005 **14** 532-542
[35] Midey A, Dotan I, Lee S, Rawlins W T, Johnson M A and Viggiano A A *Journal of Physical Chemistry A* 2007 **111** 5218-5222
[36] Volynets A V, Lopaev D V, Rakhimova T V, Chukalovsky A A, Mankelevich Y A, Popov N A, Zotovich A I and Rakhimov A T *Journal of Physics D: Applied Physics* 2018 **51** 364002
[37] Braginskiy O V, Vasilieva A N, Klopovskiy K S, Kovalev A S, Lopaev D V, Proshina O V, Rakhimova T V and Rakhimov A T *Journal of Physics D: Applied Physics* 2005 **38** 3609-3625
[38] Marinov D, Guaitella O, Booth J P and Rousseau A *Journal of Physics D: Applied Physics* 2012 **46** 032001
[39] Mazánková V, Trunec D, Krzyžánková A, Jurmanová J and Krčma F *Japanese Journal of Applied Physics* 2020 **59** SHHA02
[40] Steinfeld J I, Adler-Golden S M and Gallagher J W *Journal of Physical and Chemical Reference Data* 1987 **16** 911-951
[41] Kaufmann M, Gil-López S, López-Puertas M, Funke B, García-Comas M, Glatthor N, Grabowski U, Höpfner M, Stiller G P, von Clarmann T, Koukouli M E, Hoffmann L and Riese M *Journal of Atmospheric and Solar-Terrestrial Physics* 2006 **68** 202-212
[42] Castle K J, Black L A and Pedersen T J *The Journal of Physical Chemistry A* 2014 **118** 4548-4553
[43] Rawlins W T and Armstrong R A *The Journal of Chemical Physics* 1987 **87** 5202-5208
[44] Baulch D L, Cox R A, Hampson R F, Kerr J A, Troe J and Watson R T *Journal of Physical and Chemical Reference Data* 1980 **9** 295-472
[45] Baulch D L, Cox R A, Hampson R F, Kerr J A, Troe J and Watson R T *Journal of Physical and Chemical Reference Data* 1984 **13** 1259-1380
[46] von Rosenberg C W and Trainor D W *The Journal of Chemical Physics* 1974 **61** 2442-2456
[47] Azyazov V N, Mikheyev P, Postell D and Heaven M C *Chemical Physics Letters* 2009 **482** 56-61

[48] Ménard-Bourcin F, Ménard J and Doyennette L *The Journal of Chemical Physics* 1991 **94** 1875-1881
[49] Zeninari V, Tikhomirov B A, Ponomarev Y N and Courtois D *The Journal of Chemical Physics* 2000 **112** 1835-1843
[50] Baulch D L, Cox R A, Crutzen P J, Hampson R F, Kerr J A, Troe J and Watson R T *Journal of Physical and Chemical Reference Data* 1982 **11** 327-496
[51] Hui K K and Cool T A *The Journal of Chemical Physics* 1978 **68** 1022-1037
[52] Nikitin E E and Umanskii S Y *Theory of Slow Atomic Collisions*: Springer Berlin Heidelberg, 1984
[53] Slanger T G and Black G *The Journal of Chemical Physics* 1979 **70** 3434-3438
[54] Mankelevich Y A, Rakhimova T V, Voloshin D G and Chukalovskii A A *Russian Journal of Physical Chemistry A* 2023 **97** 1033-1045
[55] Cartry G, Magne L and Cernogora G *Journal of Physics D: Applied Physics* 2000 **33** 1303-1314
[56] Zhuravlev L T and Kiselev A V "SURFACE CONCENTRATION OF HYDROXYL GROUPS ON AMORPHOUS SILICAS HAVING DIFFERENT SPECIFIC SURFACE AREAS" *Surface Area Determination*: Elsevier 1970:155-160.
[57] Kim Y C and Boudart M *Langmuir* 1991 **7** 2999-3005
[58] Li K, Liu J and Liu W *Chinese Journal of Aeronautics* 2015 **28** 1355-1361
[59] Kondrat'Ev V N "CHAPTER 2 - CHEMICAL MECHANISM OF REACTIONS" In: V. N. Kondrat'Ev, ed. *Chemical Kinetics of Gas Reactions*: Pergamon 1964:44-115.
[60] Seebauer E and Allen C E *Progress in Surface Science* 1995 **49** 265-330
[61] Itoh H, Taguchi M and Suzuki S *Journal of Physics D: Applied Physics* 2020 **53** 185206